

Decoding the compositions of four bright *r*-process-enhanced stars

Pallavi Saraf,^{1,2*} Carlos Allende Prieto,^{3,4} Thirupathi Sivarani,¹ Avraijit Bandyopadhyay,⁵ Timothy C. Beers,^{6,7} and A. Susmitha¹

¹ Indian Institute of Astrophysics, Koramangala 2nd Block, Bangalore, 560034, India

² Pondicherry University, R.V. Nagar, Kalapet, 605014, Puducherry, India

³ Instituto de Astrofísica de Canarias, E-38200 La Laguna, Tenerife, Spain

⁴ Departamento de Astrofísica, Universidad de La Laguna, E-38205 La Laguna, Tenerife, Spain

⁵ Department of Astronomy, University of Florida, Gainesville, FL 32601, United States of America

⁶ Joint Institute for Nuclear Astrophysics-Center for the Evolution of the Elements (JINA-CEE), United States of America

⁷ Department of Physics and Astronomy, University of Notre Dame, Notre Dame, IN 46556, United States of America

Accepted XXX. Received YYY; in original form ZZZ

ABSTRACT

There has been a concerted effort in recent years to identify the astrophysical sites of the *r*-process that can operate early in the Galaxy. The discovery of many *r*-process-enhanced (RPE) stars (especially by the *R*-process Alliance collaboration) has significantly accelerated this effort. However, only limited data exist on the detailed elemental abundances covering the primary neutron-capture peaks. Subtle differences in the structure of the *r*-process pattern, such as the relative abundances of elements in the third peak, in particular, are expected to constrain the *r*-process sites further. Here, we present a detailed elemental-abundance analysis of four bright RPE stars selected from the HESP-GOMPA survey. Observations were carried out with the 10-m class telescope Gran Telescopio Canarias (GTC), Spain. The high spectral signal-to-noise ratios obtained allow us to derive abundances for 20 neutron-capture elements, including the third *r*-process peak element osmium (Os). We detect thorium (Th) in two stars, which we use to estimate their ages. We discuss the metallicity evolution of Mg, Sr, Ba, Eu, Os, and Th in *r*-II and *r*-I stars, based on a compilation of RPE stars from the literature. The strontium (Sr) abundance trend with respect to europium (Eu) suggests the need for an additional production site for Sr (similar to several earlier studies); this requirement could be milder for yttrium (Y) and zirconium (Zr). We also show that there could be some time delay between *r*-II and *r*-I star formation, based on the Mg/Th abundance ratios.

Key words: techniques: spectroscopic – Galaxy: formation – stars: abundances – stars: atmospheres – stars: fundamental parameters

1 INTRODUCTION

Understanding the formation of neutron-capture elements is one of the key topics in stellar astronomy. Since Burbidge et al. (1957) and Cameron (1957), it has been recognized that the rapid neutron-capture process (*r*-process) is one of the prime mechanisms for producing heavy elements. However, we still do not know with certainty all of the major astrophysical sites of *r*-process-enrichment in the Galaxy. Very metal-poor (VMP; $[Fe/H] \leq -2.0$) stars are expected to preserve the nucleosynthesis signatures of the first generations of stars in the Galaxy (Beers & Christlieb 2005; Frebel et al. 2005; Frebel & Norris 2015). Hence, high-resolution spectroscopy of VMP stars provides the opportunity to study the detailed chemical abundances of elements present in these stars, and thus obtain information about the production and astrophysical sites of their formation.

In the periodic table, elements up to zinc (Zn) can form in fusion reactions, but elements beyond Zn can only be formed via neutron-capture processes (Burbidge et al. 1957; Cameron 1957;

Clayton 1983; Hansen et al. 2004; Wanajo et al. 2018; Curtis et al. 2019). According to the rate of neutron capture on seed nuclei, the neutron-capture processes are conventionally divided into three classes, (1) a rapid neutron-capture process (*r*-process), (2) a slow neutron-capture process (*s*-process), and (3) an intermediate neutron-capture process (*i*-process) (Burbidge et al. 1957; Cameron 1957; Cowan & Rose 1977; Beers & Christlieb 2005; Sneden et al. 2008). The sites of enrichment of *s*- and *i*-process elements are thought to include asymptotic giant branch (AGB) stars through mass transfer from a binary companion (Herwig 2005; Campbell & Lattanzio 2008; Bisterzo et al. 2010; Doherty et al. 2015). Other suggested sources for the *s*-process involve helium core-burning massive stars (Truran & Iben 1977; Prantzos et al. 1990), carbon core-burning massive stars (Arnett & Thielemann 1985; Langer et al. 1986; Arcoragi et al. 1991), and carbon shell-burning stars (Raiteri et al. 1991). Sources for the *i*-process include post-AGB stars (Herwig et al. 2011), rapidly accreting white dwarfs (Denissenkov et al. 2017, 2019), and super-AGB stars (Jones et al. 2016).

Beers & Christlieb (2005) divided RPE stars into two categories, namely *r*-I ($+0.3 \leq [Eu/Fe] \leq +1.0$, $[Ba/Eu] < 0$), and *r*-II

* E-mail: pallavi.saraf@iiap.res.in (PS)

($[\text{Eu}/\text{Fe}] > +1.0$, $[\text{Ba}/\text{Eu}] < 0$). In the above definitions, europium (Eu) is taken as the primary indicator of *r*-process-enrichment because the abundance of Eu is dominated by the *r*-process, and is relatively easy to measure in high-resolution optical spectra. The barium (Ba) limits are introduced to remove likely *s*-process contamination. Another class of *r*-process-enhanced (RPE) stars is the so-called limited-*r* ($[\text{Eu}/\text{Fe}] < +0.3$, $[\text{Sr}/\text{Ba}] > +0.5$, and $[\text{Sr}/\text{Eu}] > 0.0$), which was introduced to account for the dispersion observed in the first peak of the *r*-process pattern (Sneden et al. 2000; Travaglio et al. 2004; Frebel 2018a). Out of all the known metal-poor stars (up to $[\text{Fe}/\text{H}] \sim -1.0$), only about 2 percent are limited-*r*, 15 percent are *r*-I, and 5 percent are *r*-II stars (Frebel et al. 2016). There are some 46 limited-*r*, 426 *r*-I, and 155 *r*-II metal-poor stars known at present (Gudin et al. 2021; Shank et al. 2023).

Several possible sites for *r*-process-element production have been proposed. These include neutrino-driven winds in Type-II supernovae (Woosley & Hoffman 1992; Takahashi et al. 1994; Arcones et al. 2007; Wanajo et al. 2018), the prompt explosion of low-mass supernovae (Wheeler et al. 1998; Sumiyoshi et al. 2001; Wanajo et al. 2003), neutron star – neutron star or neutron star – black hole mergers (Lattimer & Schramm 1974, 1976; Symbalisty & Schramm 1982; Meyer 1989; Freiburghaus et al. 1999; Goriely et al. 2011; Rosswog et al. 2014; Bovard et al. 2017), and collapsars (Woosley 1993; Nagataki et al. 2007; Fujimoto et al. 2008; Siegel & Metzger 2018; Siegel et al. 2019). The neutrino-driven winds in Type-II supernovae model over-produce elements near atomic mass A~90 and require a level of entropy to produce *r*-process elements higher than predicted in hydrodynamical simulations (Takahashi et al. 1994). The problem with the prompt explosions of low-mass supernovae model is whether it really explodes or not (Bethe 1990; Sumiyoshi et al. 2001). The collapse of a rapidly rotating massive star can lead to the formation of an accretion disc around the remnant black hole – a collapsar – and has been shown to be a potential candidate for *r*-process-element production (Siegel et al. 2019). All of these proposed sites are limited by various factors that remain to be verified by observations (and simulations). Given these uncertainties, the actual astrophysical site or sites of *r*-process enrichment is still a topic of debate.

Observations of the electromagnetic counterparts of binary neutron star mergers detected by the LIGO-Virgo collaboration exhibited a kilonova-like behaviour (Arcavi et al. 2017; Smartt et al. 2017; Tanvir et al. 2017). The excess red emission from the kilonova lightcurve and the detection of a strontium (Sr) spectral feature provide direct evidence for neutron star mergers as one of the robust sites of *r*-process element production (Chornock et al. 2017; Drout et al. 2017; Metzger 2017; Shappee et al. 2017; Tanaka et al. 2017; Villar et al. 2017; Watson et al. 2019).

A single neutron star merger (NSM) event can enrich a large number of stars with *r*-process-element ejecta, as observed in the *r*-process-rich ultra-faint dwarf galaxy Reticulum II (Ret II) (Ji et al. 2016, 2022; Roederer et al. 2016). We point out that Ji et al. (2022) reports that over 70 percent of the stars in Ret II with available high-resolution spectroscopic follow-up indicate strong enrichment by *r*-process elements. However, there remain several difficulties in our understanding. The long delay between the first supernovae explosions that produce Mg, Fe-peak elements, and ejection of *r*-process material from NSMs, for instance, does not support the observed *r*-process-enhancement by NSM in a pristine galaxy (Argast et al. 2004; Wehmeyer et al. 2015; Tarumi et al. 2021). The presence of large numbers of Eu-rich stars at low metallicity (see, e.g., Holmbeck et al. 2018) and the trend between $[\text{Eu}/\text{Fe}]$ and $[\text{Fe}/\text{H}]$ for Milky Way stars also does not match with the simulations us-

ing NSMs as the primary site for *r*-process-element production (Argast et al. 2004; Wehmeyer et al. 2015). However, there have been efforts to explain *r*-process enrichment at low metallicity with accretion of stars from low-mass dwarf galaxies (Hirai et al. 2015, 2022) and neutron star natal kicks (Banerjee et al. 2020).

Detailed abundances covering the full range of the *r*-process-element patterns for larger samples of stars clearly assist in efforts to constrain the sites of *r*-process-element production. In this work, we derive elemental abundances for 20 neutron-capture elements in four bright RPE stars. We compare their elemental-abundance trends with a compiled list of RPE and “normal” halo stars. We also discuss possibly interesting trends in the abundance ratios.

This paper is outlined as follows. In Section 2, we discuss the observations, telescope, and the high-resolution spectrograph we employ. Data reduction and radial velocity determinations are provided in Section 3. Stellar-parameter estimation using different methods is discussed in Section 4. The detailed chemical abundances of our four program stars are briefly discussed in Section 5. Sections 6 and 7 are discussions of our main results and a summary of the key conclusions.

2 OBSERVATIONS

In this study, we have selected four relatively bright ($V < 12$) RPE VMP stars from Bandyopadhyay et al. (2020b) [part of HESPGOMPA survey (Bandyopadhyay et al. 2020a)] to obtain high signal-to-noise ratio (SNR) spectra, including the bluer spectral wavelengths that previously had too low SNRs for detailed study, to determine elemental abundances and upper limits of as many elements as possible, and to probe the rare-earth peak elements. These stars were initially selected from the SDSS-III MARVELS radial velocity survey (Ge et al. 2015).

Observations were carried out using the High Optical Resolution Spectrograph (HORuS) installed on the Gran Telescopio Canarias (GTC) (Tabernero et al. 2020; Allende Prieto 2021). The GTC is a 10-m class telescope situated at the Roque de Los Muchachos Observatory on the island of La Palma, in the Canaries, Spain. HORuS is located at the Nasmyth focal plane of the telescope, and provides simultaneous wavelength coverage (3800 – 6900 Å) at a spectral resolution of $R \sim 25000$. The observations were obtained in the month of December, 2019. During the observations, we obtained the sets of bias and flat frames required for data-reduction procedure. We also obtained several Th-Ar lamp spectra for the wavelength calibration of the object spectra. All the useful information related to our program stars, including the name of the star, right ascension (RA), declination (DEC), *V*-band magnitude, with calculated SNR per pixel around the 4500 Å region, exposure time, and date of observation are listed in Table 1.

3 DATA REDUCTION AND RADIAL VELOCITY DETERMINATIONS

3.1 Data Reduction

We employ standard procedures for the spectroscopic data reduction of our program stars. First, all the spectra are corrected for bias using a median bias frame, followed by cosmic ray removal and scattered light correction. Then we perform a flat-fielding operation to correct the non-uniform pixel-to-pixel sensitivity of the detector. Wavelength calibration is accomplished using Th-Ar lamp spectra obtained with the same spectroscopic setup as that of the object.

Table 1. Basic information for our program stars. The spectral coverage is 3800–6900 Å, and exposure times for each object were 1800 seconds, with two exposures of 900 seconds. The equinox and epoch for the coordinates is J2000.

Star name	RA	DEC	V mag	SNR	Date of Observation (UT)
TYC 3431-689-1	09:21:57.28	+50:34:04.5	11.75	102 (4500 Å)	2019/12/22
HD 263815	06:48:13.33	+32:31:05.2	9.92	161 (4500 Å)	2019/12/23
TYC 1191-918-1	00:43:05.28	+19:48:59.1	9.90	107 (4500 Å)	2019/12/26
TYC 1716-1548-1	23:19:23.84	+19:17:15.4	11.57	126 (4500 Å)	2019/12/26

Finally, we normalized the continuum of the spectra to unity. All data-reduction operations were performed within the IMRED, CC-DRED, and ECHELLE packages of NOAO’s Image Reduction and Analysis Facility (IRAF)¹.

3.2 Radial Velocities

Radial velocities (RVs) of our program stars with respect to the observer’s frame of reference are calculated by cross-correlating the observed spectra with a template synthetic spectrum with similar stellar parameters. We performed the cross-correlation task using the IDL routine CRSCOR for each spectral order in the entire spectral range from 3800 to 6900 Å. We take the median of radial velocities of these orders as the geocentric radial velocity of the star and their standard deviation (σ) as the error in the radial velocity.

All the continuum-normalized spectra were corrected for the Doppler shift due to the radial velocities of the stars using the IRAF task DOPCOR. Table 2 lists the geocentric RVs and the heliocentric RVs of our program stars corrected for the motion of the Earth around the Sun, the Gaia DR3 RVs (Gaia Collaboration 2022), and the RVs reported by Bandyopadhyay et al. (2020b); the RVs reported by the latter source were geocentric. In this paper, we have corrected their RVs for the motion of earth around the Sun and report heliocentric RVs. Our RV calculations are in good agreement with the recent Gaia DR3 values. There is no apparent variation in RV that might indicate binaries among our targets.

4 LINE LIST AND STELLAR PARAMETERS

4.1 Line List

For an accurate determination of stellar parameters, we have restricted ourselves to spectral lines using the following selection criteria:

- (i) Blended and asymmetric lines are avoided, due to potential contamination by other lines or species.
- (ii) Lines without clear continua are avoided, due to the difficulty of modeling the overly crowded regions of the spectrum.
- (iii) Lines with equivalent widths below 20 mÅ and above 120 mÅ are avoided; below 20 mÅ the lines are often dominated by noise, and above 120 mÅ they can approach saturation.

We employ the above criteria for all of our program stars. Appendix B provides a combined Fe line list for all the stars. The values of the lower excitation potential (LEP), the $\log g f$, and the measured equivalent widths are listed in this table.

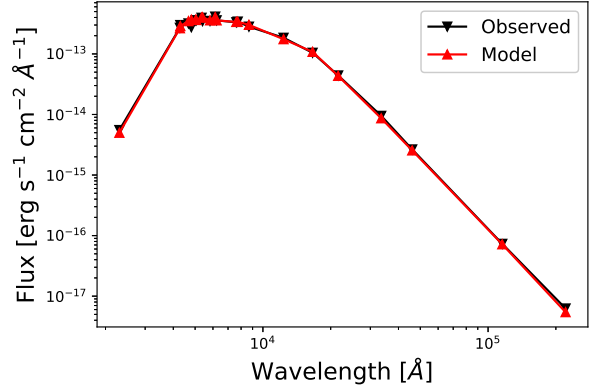


Figure 1. Temperature estimation using SED fitting for one of our program stars, HD 263815. The observed SED is shown with black downward triangles connected by a black line; the fitted SED is represented with red upward triangles, fitted with the red curve.

4.2 Stellar Parameters

We employ both photometric and spectroscopic measurements for estimation of the stellar parameters (effective temperature: T_{eff} , surface gravity: $\log g$, micro-turbulence velocity: ξ , and metallicity: [Fe/H]) of our program stars. Here we discuss in detail the approaches we use.

4.2.1 Photometry

Photometric colours, the spectral energy distribution (SED), and Gaia photometry (Gaia Collaboration et al. 2021) are used to estimate the photometric temperatures. We use the extinction-corrected colours (Schlafly & Finkbeiner 2011) with the temperature-colour relations described in Alonso et al. (1999) for temperature estimation. For the SED-based temperature estimation, we employ the SED-fitting web tool Virtual Observatory SED Analyzer (VOSA)². VOSA provides several theoretical stellar models to fit the SED, obtained from various photometric surveys that are publicly available (Bayo et al. 2008). For each star we apply a Bayesian analysis and chi-square fitting to obtain the temperature estimate. Fig. 1 shows an example of SED fitting for one of our program stars, HD 263815. Temperature estimates obtained from various photometric techniques are listed in different columns of Table 3.

4.2.2 Spectroscopy

To estimate the stellar parameters using spectroscopic methods, we have identified Fe I and Fe II absorption lines in the spectra, taking

¹ <https://iraf-community.github.io>

² <http://svo2.cab.inta-csic.es/theory/vosa/>

Table 2. Radial velocities of our program stars.

Star name	Geocentric RV (km/s)	Heliocentric RV (km/s)	Error (km/s)	RV GAIA DR3 ^(a) (km/s)	RV HESP ^(b) (km/s)
TYC 3431-689-1	-127.98	-112.95	0.28	-110.75±0.44	-111.96±0.50
HD 263815	133.99	139.33	0.52	138.74±0.23	136.13±0.41
TYC 1191-918-1	-158.01	-186.96	0.19	-187.46±0.18	-189.26±0.51
TYC 1716-1548-1	-250.00	-278.27	0.43	-277.10±0.20	-277.89±0.47

^a Gaia Collaboration (2022)^b Bandyopadhyay et al. (2020b) [we have listed here heliocentric RVs after correction.]**Table 3.** Estimate of effective temperature (T_{eff} , in K) of our program stars, using different photometric and spectroscopic methods.

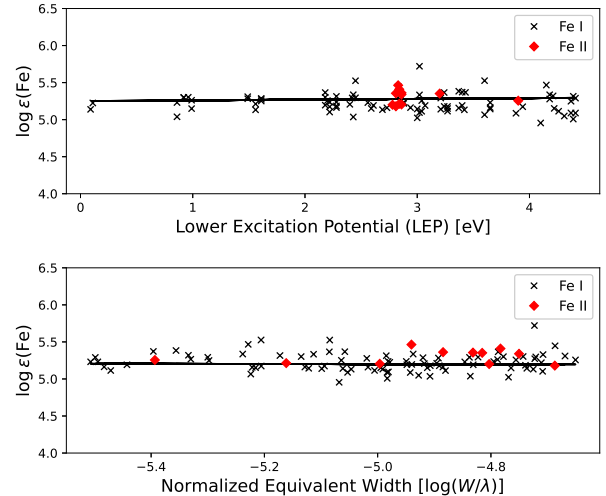
Star name	H α	V-K	J-K	J-H	Fe-I	SED	GAIA
TYC 3431-689-1	4900	5017	4938	4754	4850	5000	5450
HD 263815	4700	4872	4809	4874	4700	4750	5016
TYC 1191-918-1	4700	4690	4613	4756	4650	4750	4877
TYC 1716-1548-1	4550	4522	4286	4362	4500	4500	4644

into account the criteria mentioned in Section 4.1. Traditionally, Fe lines are used to estimate the stellar parameters due to their ubiquitous presence in optical spectra. Our selection criterion results in 110 Fe I and 17 Fe II lines for TYC 3431-689-1, 102 Fe-I and 18 Fe-II lines for HD 263815, 111 Fe-I and 20 Fe-II lines for TYC1716-1586-1, and 106 Fe-I and 21 Fe-II lines for TYC 1191-918-1. The equivalent width (EW) of each line is calculated interactively by Gaussian fitting of the line in the SPLOT task of IRAF. For a consistency check, we have also calculated the equivalent widths using an automated code, the Automatic Routine for line Equivalent widths in stellar Spectra (ARES; Sousa et al. 2007). Due to the good signal-to-noise of the spectra, both methods provide consistent results.

After line identification, we generated a grid of model stellar atmospheres using ATLAS9 (Kurucz 1993; Castelli & Kurucz 2003). We used the spectrum synthesis code TURBOSPECTRUM (Alvarez & Plez 1998; Plez 2012) for abundance calculation of Fe I and Fe II lines, which were later used for the estimation of stellar parameters. The same codes are used for the abundance estimation of other elements in Section 5.

Spectroscopic temperature estimates are obtained by assuming excitation equilibrium among the neutral iron lines, i.e., by demanding that the abundance of Fe I lines is independent of the lower excitation potential (LEP), as shown in the top panel of Fig. 2. We have also fitted the wings of the H α absorption profile to obtain an independent estimate, as they are highly sensitive to small changes in temperature. As an illustration, the H α wing-fitting results are shown in Fig. 3. Note that the primary purpose of this exercise is to fit the wings of the H α line to check the consistency in temperature estimates. Thus, we have only shown the wings of H α line for clear visibility (see, Sahin & Lambert 2009; Matsuno et al. 2017). Also, fitting of the H α line requires full 3D non-LTE (NLTE) modeling, as the core part of the line forms in the upper atmosphere, whereas the wings form deep in the photosphere (Leenaarts et al. 2012).

Stellar surface gravity is estimated presuming the ionization balance of an element, i.e., by forcing the abundance of an element in its neutral state (Fe I) and ionized state (Fe II) to be the same by changing the surface gravity. We also fit the wings of the magnesium (Mg) triplet (5167Å, 5172Å, 5187Å) to obtain an estimate of log g , because the Mg-triplet wings are sensitive to small changes

**Figure 2.** Top: Iron abundance, as a function of lower excitation potential (LEP). Bottom: Iron abundance, as a function of normalized equivalent width, for one of our program stars, HD 263815.

in surface gravity. As an illustration, Fig. 4 shows fits for portions of the Mg-triplet region. For a consistency test, we place our program stars on stellar isochrones ranging from 8 to 12 Gyr in age. These isochrones are obtained from the CMD 3.6 website³, which uses PARSEC (Bressan et al. 2012) and COLIBRI (Marigo et al. 2013) tracks. Fig. 5 shows the isochrones and our program stars.

It is customary to use the abundance of iron (Fe) as an indicator of stellar metallicity. The absolute abundances are calculated on a log scale, with the number density of H assumed to be 12; relative abundances are calculated with respect to the solar ratio⁴. In this work, we have used solar abundances from Asplund et al. (2009). Table 5 lists metallicities for all of our program stars.

³ <http://stev.oapd.inaf.it/cgi-bin/cmd>⁴ Absolute abundance of element A: $\log \epsilon(A) = \log(N_A/N_H) + 12$ and the relative abundance of element A with respect to element B: $[A/B] = \log(N_A/N_B) - \log(N_A/N_B)_{\odot}$, where \odot represents values for the Sun.

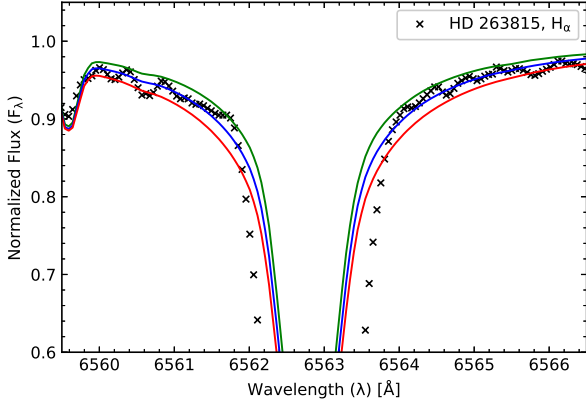


Figure 3. H α wing fitting for one of our program stars, HD 263815. The blue colour represents the best fit at a temperature of 4700 K; 150 K deviations in T_{eff} from the best fit are shown with green and red colours.

Table 4. Estimates of micro-turbulence velocity (ξ) of our program stars using the methods described in the text.

Star name	using abundance of Fe I & Fe II lines (km/s)	using dispersion of Fe I abundance (km/s)
TYC 3431-689-1	1.80	2.00
HD 263815	1.85	1.90
TYC 1191-918-1	1.95	2.10
TYC 1716-1548-1	1.95	2.00

To calculate the micro-turbulence velocity, we force the abundance of neutral iron lines (Fe I) to be independent of reduced equivalent width ($\log[EW/\lambda]$), as shown in the bottom panel of Fig. 2. For an additional check, we also calculate an estimate of the micro-turbulence velocity using the method described in Sahin & Lambert (2009), Reddy et al. (2012), and Molina et al. (2014), which makes use of the dispersion in the abundance of an element. The value of micro-turbulence where the dispersion becomes a minimum is taken as the micro-turbulence velocity of the atmosphere. For this analysis, we used the abundances of Ti I, Ti II, Cr I, Cr II, Fe I, Fe-II, V I, and V II, depending on the presence of significant numbers of clean lines in the spectra. For example, Fig. 6 shows the dispersion in the elemental abundance of Fe I lines for one of our program stars, HD 263815. The minimum of the distribution is the estimated micro-turbulence velocity in the stellar atmosphere. Table 4 lists micro-turbulence velocities of our program stars using the above methods. For further analysis, we have restricted ourselves to the stellar parameters obtained using the spectroscopic method, i.e., T_{eff} from excitation equilibrium, $\log g$ from ionization balance, micro-turbulence from zero trend of Fe I with normalized equivalent width, and metallicity from the mean Fe I abundance. The final adopted stellar parameters for our program stars are listed in Table 5. Our parameters are in good agreement with those from Bandyopadhyay et al. (2020b), except for the metallicities. We identified the likely reason for this discrepancy as due to systematically lower values for equivalent widths obtained by the previous authors (used by them primarily for the Fe-peak elements).

Table 5. Final adopted stellar parameters for our program stars.

Star name	T_{eff} (K)	$\log g$	[Fe/H]	ξ (km/s)
TYC 3431-689-1	4850	1.4	-2.05	1.80
HD 263815	4700	1.3	-2.22	1.85
TYC 1191-918-1	4650	1.1	-1.90	1.95
TYC 1716-1548-1	4500	1.2	-2.15	1.95

5 ABUNDANCE ANALYSIS

In this study, we use a combination of equivalent-width analysis and spectrum synthesis methods for the elemental-abundance estimates. For the lighter elements, up to Zn, one can easily find unblended lines in our spectra. Thus, we use the equivalent-width method, but also carried out spectrum synthesis for some of the lines to check the consistency. In the case of heavier elements, most of the absorption features contain contributions from other atomic transitions, thus spectrum synthesis is performed for them.

In the equivalent-width analysis we select lines with equivalent widths $< 120 \text{ m}\text{\AA}$, which are on the linear part of the Curve of Growth, and are not sensitive to the broadening of the wings. Note that we have dropped the lower-limit criterion of $20 \text{ m}\text{\AA}$ to study more elements and lines. For each element, we have used the solar abundances from Asplund et al. (2009). We have also incorporated the hyperfine-splitting information for Sc, V, Mn, Cu, Ba, La, Pr, Nd, Sm, and Eu. Solar isotopic ratios are employed.

5.1 Light Elements: Molecular Bands (Carbon and Nitrogen)

We estimate carbon (C) abundances from the CH *G*-band molecular region around 4313 \AA , which could be obtained for all of our program stars using the spectrum-synthesis method. We have used the line list from Masseron et al. (2014) for CH band synthesis. The top panel of Fig. 7 shows the observed spectrum using black dots and the best-fit synthetic spectrum using a blue colour line for one of our program stars, HD 263815. The green and red colours indicate ± 0.5 dex deviations from the best-fit synthesis line. We have also attempted to constrain the $^{12}\text{C}/^{13}\text{C}$ ratio. For this purpose, we performed spectral synthesis in 4211 \AA , 4230.30 \AA and 4231.45 \AA regions. Our analysis shows that the average $^{12}\text{C}/^{13}\text{C}$ is 3.0 for TYC 3431-689-1, 3.5 for HD 263815, 5.5 for TYC 1191-918-1, and 5.5 for TYC 1716-1548-1. Due to the high SNRs of our spectra in the blue region, we could also evaluate the nitrogen (N) abundances for all four of our program stars. The line list for CN band is adopted from Plez & Cohen (2005). We use the CN-band molecular region around 3883 \AA for calculating the abundance of N. We performed the spectral synthesis of the CN band by keeping the carbon abundance fixed at the value obtained from the CH *G*-band. An example of the CN-band synthesis is shown in the bottom panel of Fig. 7.

Our program stars exhibit relatively low surface carbon abundances, as expected from their current evolutionary stages. All four stars fall in the red giant region, indicating that their C abundances have been depleted during evolution up the red giant branch. We use the method described in Placco et al. (2014b) to correct the observed carbon abundances for the evolutionary states of the stars. Table 6 lists the LTE values of the observed C abundances from our analysis, along with their corrected C abundances.

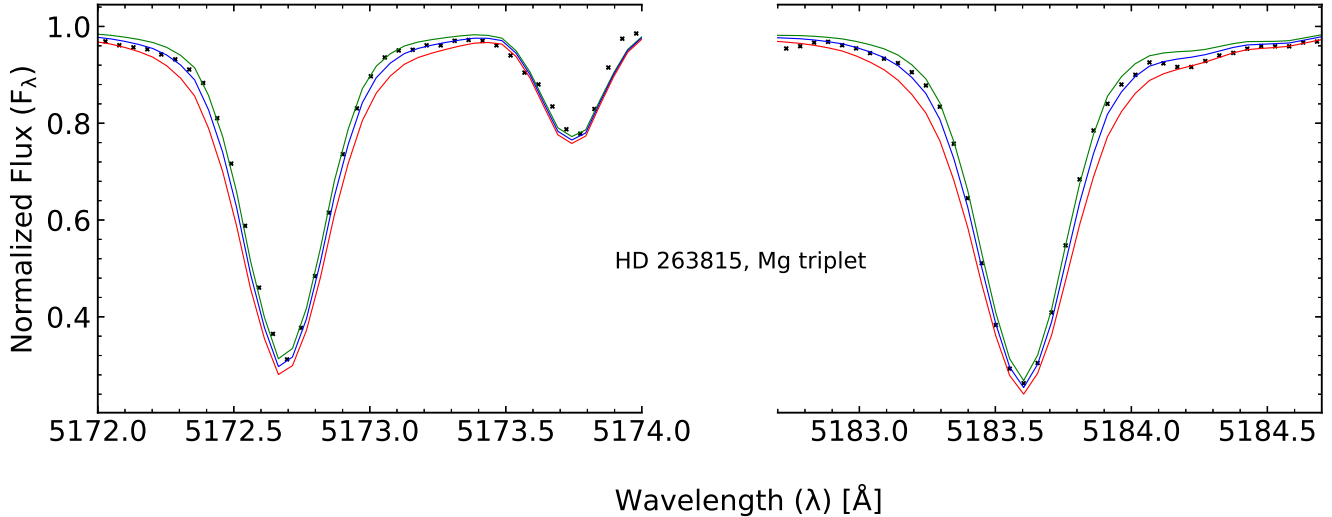


Figure 4. Mg-triplet wing fitting for one of our program stars, HD 263815. The best-fit line is shown with blue colours; 0.3 dex deviations from the best fit are shown with green and red lines.

Table 6. Dilution of carbon corrected according to Placco et al. (2014b), and *r*-process classification of our program stars from Holmbeck et al. (2020).

Star name	[Fe/H]	[C/Fe] _{LTE}	Δ [C/Fe] _{cor} ^a	[C/Fe] _{cor}	[Sr/Fe]	[Ba/Fe]	[Eu/Fe]	[Ba/Eu]	[Sr/Ba]	Class
TYC 3431-689-1	-2.05	-0.60	+0.55	-0.05	+0.15	+0.25	+0.80	-0.55	-0.10	<i>r</i> -II
HD 263815	-2.22	-0.58	+0.63	+0.05	-0.18	-0.13	+0.52	-0.65	-0.05	<i>r</i> -I
TYC 1191-918-1	-1.90	-0.70	+0.66	-0.04	-0.10	-0.14	+0.55	-0.69	+0.04	<i>r</i> -I
TYC 1716-1548-1	-2.15	-0.35	+0.62	+0.27	+0.15	+0.17	+0.80	-0.63	-0.02	<i>r</i> -II

^a <https://vplacco.pythonanywhere.com/>.

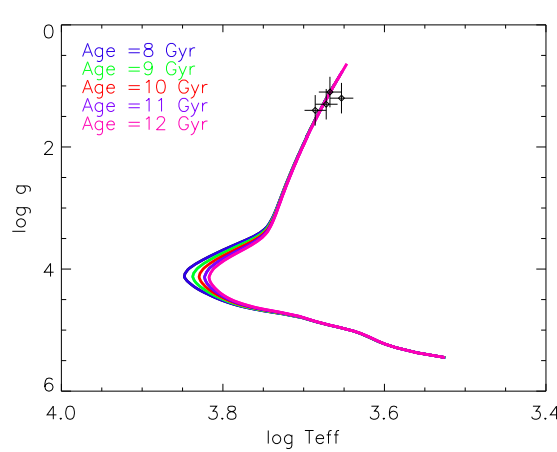


Figure 5. Surface gravity ($\log g$) vs. effective temperature ($\log T_{\text{eff}}$) for our program stars. The black diamonds show the locations of the program stars along with the measurement uncertainties. Different colour curves shows isochrones ranging 8 to 12 Gyr in age.

5.2 Alpha-elements: Mg, Si, Ca, Ti

We have identified the α -elements Mg, Si, Ca, and Ti in our program stars. In all the stars, we identified numerous clean Ti I and Ti II lines, so the Ti abundance was calculated using the equivalent-width method. Although there are significant numbers of Ca I lines present

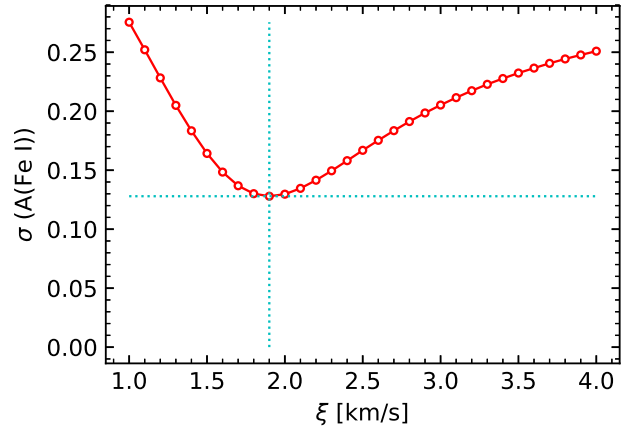


Figure 6. Micro-turbulence velocity estimation using dispersion in the abundances of Fe I lines for one of our program stars, HD 263815. Here, the crossing point of vertical and horizontal lines represents the minimum of the distribution. The micro-turbulence value that corresponds to this crossing point is taken as its estimate in the stellar atmosphere.

in the spectra, we used both the equivalent-width and spectrum-synthesis methods for Ca abundance estimation. Abundances of Mg and Si were determined using the spectrum-synthesis method. We derive the Si abundance using the 4102 Å and 6155 Å lines.

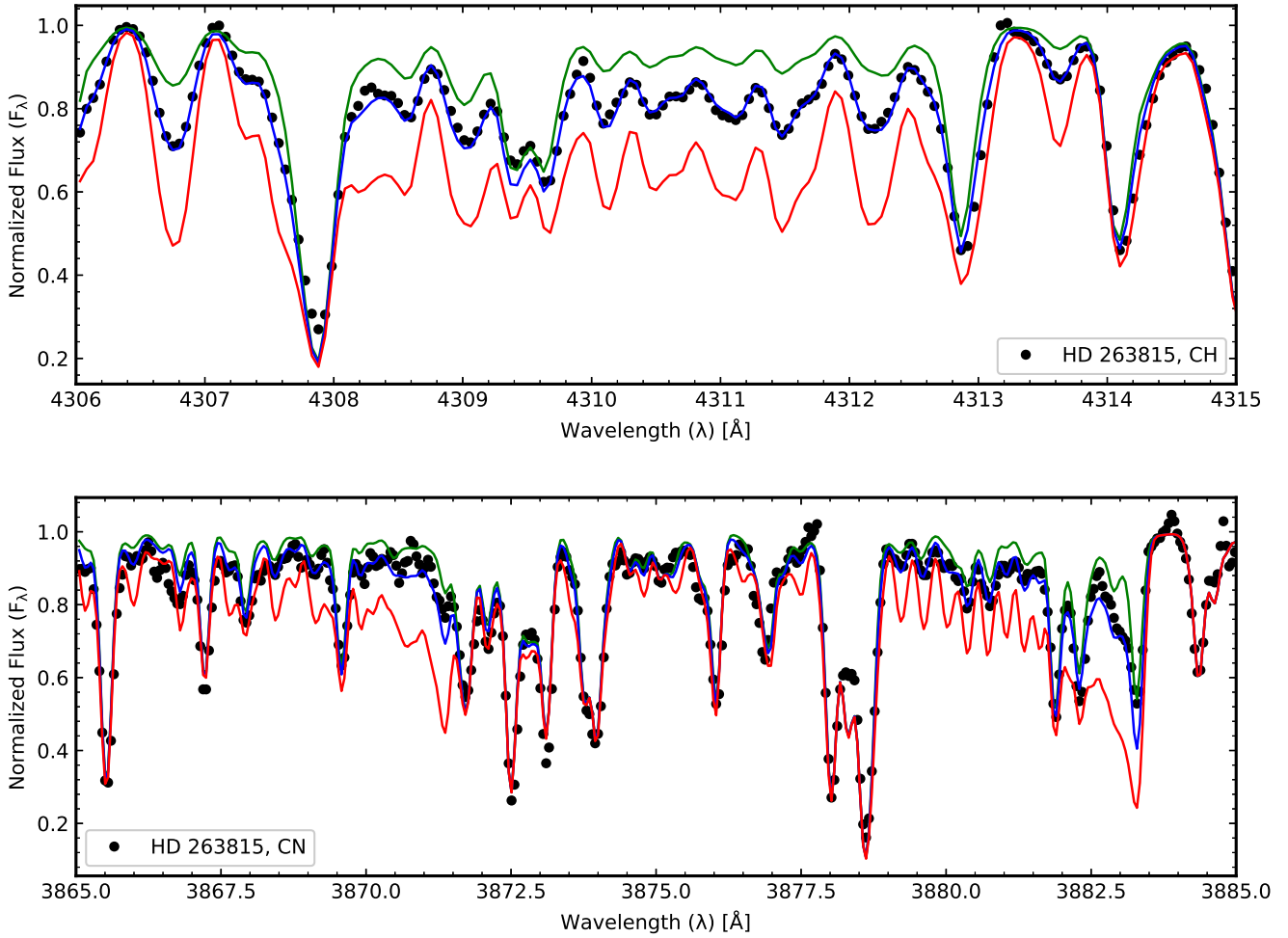


Figure 7. C and N abundance estimation for one of our program stars, HD 263815, using the spectrum-synthesis method. The top and bottom panels show the C and N synthesis, respectively. The black dotted points represent the observed spectra and the solid blue colours show the best fit. The green and red colours indicate ± 0.5 dex deviations from the best fit.

5.3 Odd-Z Elements: Na, Al

Among the odd-Z elements, we could calculate the abundances of sodium (Na) and Aluminium (Al). The sodium D1 and D2 lines at 5890 Å and 5896 Å, respectively, are used to calculate the abundance of Na. The abundance of Al is derived from the resonance lines present at 3941 Å and 3961 Å. These four lines are strongly affected by NLTE effects, so we have taken into account these corrections (Baumueller & Gehren 1997; Gehren et al. 2004; Andrievsky et al. 2007, 2008; Lind et al. 2011). Proper care has been taken for the Na synthesis in accordance to Barklem & O’Mara (2001) for line broadening due to collisions. Fig. 8 shows the synthesis of the Na I line at 5890 Å to demonstrate the spectral synthesis considering collisional broadening. We have also verified the consistency of our estimated Na and Al abundances with those of other halo stars.

5.4 Iron-peak Elements: Sc, V, Cr, Mn, Fe, Co, Ni, Cu, Zn

We have calculated the abundances for some of the iron-peak elements Sc II, V I, V II, Cr I, Cr II, Mn I, Fe I, Fe II, Co I, Ni I, Cu I, and Zn I. A mix of both the equivalent-width method and the spectrum-synthesis method are used for abundance estimation. Hyperfine splitting is also considered wherever required. Iron (Fe

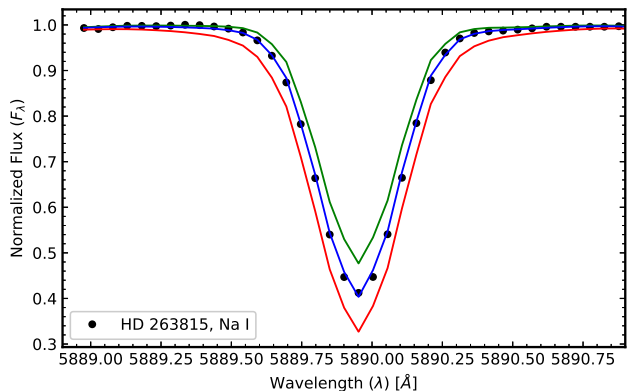


Figure 8. Synthesis of the Na-absorption feature. The black dotted points represent the observed spectra and the solid blue colour shows the best fit. Green and red colours indicate ± 0.5 dex deviations from the best fit.

I and Fe II) abundances are calculated using the equivalent-width method during the stellar-parameter estimation procedure.

Abundances of Co, Cu, and Zn are determined using the

spectrum-synthesis method. We found only one line, at 5105.53 Å, useful for Cu abundance estimation. The Co abundance was evaluated using the 5020.82 Å, 4110.53 Å, and 4121.31 Å lines. We use the 4810.52 Å, and 4722.15 Å lines for the Zn-abundance calculation. Tables A1, A2, A3, and A4 list the derived abundances of the iron-peak elements and the number of lines used for their estimation. All the abundances are consistent with previous estimates for halo stars.

5.5 Neutron-capture Elements

The absorption lines of neutron-capture elements are often blended with other elements. Sometimes they possess hyperfine structure as well. Thus, we use the spectrum-synthesis method for the abundance estimation of neutron-capture elements. We have identified a total of 20 neutron-capture elements: Sr, Y, Zr, Ba, La, Ce, Pr, Nd, Sm, Eu, Gd, Tb, Dy, Ho, Er, Tm, Lu, and Hf, and some important third *r*-process peak elements like Os and Th. Note that some elements may or may not be present in all of our program stars. In this study, the abundances of 10 elements (Pr, Gd, Tb, Ho, Er, Tm, Lu, Hf, Os, Th) of the 20 considered have been derived for the first time for our program stars.

5.5.1 First-peak elements

We obtain measurements of the absorption lines for three first-peak *r*-process elements: Sr, Y, and Zr. The abundance of Sr is estimated from two lines at 4077 Å, and 4215 Å. Both of these lines yielded very similar abundances. We have also estimated Sr abundance using the Sr I line present at 4607 Å, and found that it yields significantly lower abundance because of NLTE effects (Bergemann et al. 2012). Therefore, we have not considered it for the average abundance calculation of Sr. The abundances of Y and Zr are estimated using 7 transitions for each element. Fig. 9(a) shows the synthesis of the Sr line in the 4215 Å wavelength region. Similar to many RPE stars, the first *r*-process peak does not match very well with the scaled-solar *r*-process pattern (see Fig. 18).

5.5.2 Second-peak elements

In the second-peak region of the *r*-process pattern, we have detected a total of 15 elements: Ba, La, Ce, Pr, Nd, Sm, Eu, Gd, Tb, Dy, Ho, Er, Tm, Lu, and Hf. We were unable to measure Pr and Hf in TYC 1716-1548-1, and no Gd, Ho, and Er measurements were possible in TYC 1191-918-1. The element Tb was only measured in HD 263815 and TYC 3431-689-1, while Tm was available only in HD 263815. All the information related to the identified lines is listed in appendix C.

The abundance of Ba is estimated using the lines at 4554 Å, 4934 Å, 5853 Å, 6142 Å, and 6496 Å. The line at 4934 Å is blended with an Fe I line whose $\log g f$ is not well-constrained (Gallagher et al. 2012; Hansen et al. 2018b). We have corrected the abundance derived from the line at 4554 Å for NLTE effects from Short & Hauschildt (2006), where the authors showed a maximum NLTE correction of +0.14 dex at $[\text{Fe}/\text{H}] = -4.0$. Fig. 9(b) shows the synthesis for one of the Ba lines at 4554 Å. The Eu abundance is primarily derived from the two lines at 4129 Å and 4205 Å. Both these lines yield very similar abundance estimates. Fig. 9(c) shows the spectrum synthesis for the Eu line at 4129 Å. We estimated Tb and Lu abundances using spectrum synthesis of lines at 3976 Å and 5476 Å, respectively. Fig. 9(d) and Fig. 10(b) show the synthesis of

Table 7. Line list used for the spectrum synthesis of Th II lines in the 4019.129 Å region.

Species	wavelength (Å)	$\log g f$	LEP (eV)
Nd II	4018.823	-0.899	0.064
Cr I	4018.826	-2.629	3.648
Cr I	4018.863	-2.822	4.440
V I	4018.929	-0.651	2.581
Mn I	4018.999	-1.497	4.354
V II	4019.036	-2.704	3.753
Fe I	4019.042	-2.780	2.608
Fe I	4019.052	-2.78	2.608
Ce II	4019.057	-0.213	1.014
Ni I	4019.058	-3.174	1.935
Fe II	4019.110	-3.102	9.825
Co I	4019.126	-2.270	2.280
Th II	4019.129	-0.228	0.000
V I	4019.134	-1.999	1.804
Co I	4019.163	-3.136	2.871
Fe II	4019.181	-3.532	7.653
Co I	4019.289	-3.232	0.582
Co I	4019.299	-3.769	0.629
Cr II	4019.289	-5.604	5.330
¹² CH	4019.440	-7.971	1.172

the Tb II and Lu II lines, respectively. Abundances of all the second-peak *r*-process elements are listed in Tables A1, A2, A3, and A4. These are in good agreement with the scaled-solar *r*-process pattern (see Fig. 18).

5.5.3 Third-peak elements

We have estimated the abundances of two important elements (Os and Th) in the third *r*-process peak. The Os abundance is derived from two lines in the 4420 Å and 4265 Å regions. We have performed synthesis of the two Os lines shown in Fig. 9(e), and 10(a). The Th abundance is estimated using one strong line present in the spectra in the 4019 Å region. It is highly blended with several other lines, such as V, Fe, Co, Ni, Ce, Nd, etc., along with the molecular CH *G*-band. We took care of all the blends while synthesizing Th. First, we estimated the abundances of blended elements using clean lines present in the other parts of the spectrum. Then we fixed the abundances of these blends and varied the Th abundance to match the observed spectrum with a synthetic spectrum. Table 7 lists all the lines used for the Th II 4019 Å region synthesis (references, Johnson & Bolte 2001; Hayek et al. 2009; Ren et al. 2012). We could obtain an upper limit for lead (Pb) for three of our program stars. Fig. 9(f) shows the synthesis of Th in TYC 3431-689-1. To test the robustness of our Th determination in the spectra, we compute equivalent widths of all the contributing elements in the 4019.00–4019.44 Å range. We found the contributions of Th in this absorption line is 44 percent for TYC 3431-689-1 and 59 percent for TYC 1191-918-1. Due to the low signal-to-noise ratio ($\text{SNR} < 15$) in the 3959 Å region, we could not detect U in our program stars. The highly RPE stars with low $[\text{C}/\text{Fe}]$ would be good candidates for U detection using GTC.

5.6 Uncertainties in Abundances

The calculation of elemental abundances requires stellar parameters and the line list as inputs. The stellar parameters from spectroscopic methods also need an atomic line list as input. Each line

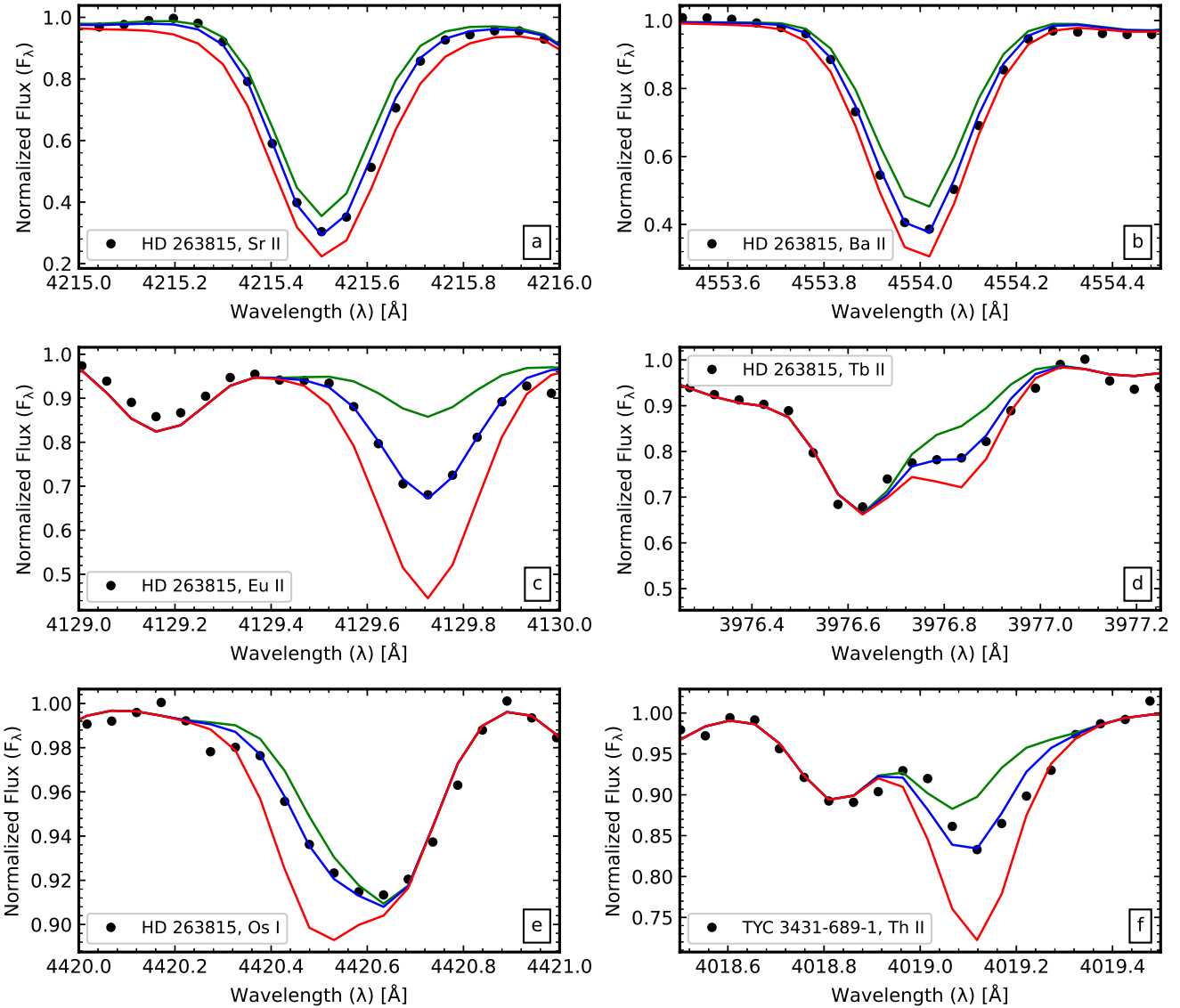


Figure 9. Synthesis of Sr, Ba, Eu, Tb, Os, and Th. The black dotted points represent the observed spectra and the solid blue colour shows the best fit. Green and red colours indicate ± 0.5 dex deviations from the best fit.

has some intrinsic uncertainty in the atomic/molecular data and the line parameters, which propagates all the way to the estimation of elemental abundances. The SNR of the spectrum also contributes to this uncertainty (Cayrel 1988). In this study, we calculate errors in our abundance estimation assuming a 150 K uncertainty in T_{eff} , and a 0.25 dex uncertainty in $\log g$. Errors due to the SNR ratio are computed using the expression given in Cayrel (1988). The total error in the elemental abundance is given as a quadratic sum of all the errors.

6 DISCUSSION

6.1 Level of *r*-process Enhancement and Classification

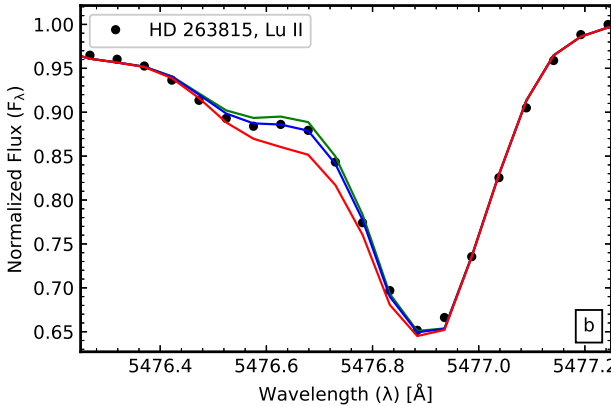
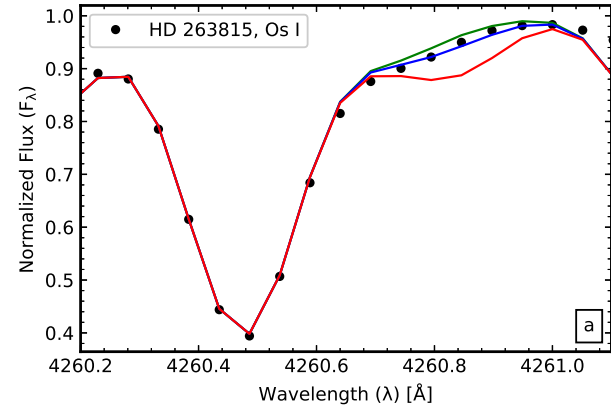
Traditionally, abundances of C, Fe, Sr, Ba, and Eu are used to classify metal-poor stars into several categories according to the enhancement level of these elements. Europium is often used as an indicator of the *r*-process, while Ba is often taken as an indicator

of the *s*-process. Classifications of metal-poor stars were initially provided by Beers & Christlieb (2005), and modifications were suggested by (Frebel 2018a). Cain et al. (2020) added a class of *r*-III stars to include extremely RPE stars with $[\text{Eu}/\text{Fe}] > +2.0$. Recently, Holmbeck et al. (2020) updated the *r*-process classification using a large sample of RPE stars from the RPA survey, most notably shifting the dividing line between *r*-I and *r*-II stars to $[\text{Eu}/\text{Fe}] = +0.7$ based on a statistical analysis, which we adopt for the rest of this paper. These classifications are listed in Table 8. Some mildly RPE stars exhibit excess abundances of the first *r*-process peak elements that could be the result of a limited-*r* process, defined as $[\text{Eu}/\text{Fe}] < +0.3$, $[\text{Sr}/\text{Ba}] > +0.5$, and $[\text{Sr}/\text{Eu}] > 0.0$ (Frebel 2018a) and employed by Holmbeck et al. (2020). The common presence of C-enhancement in VMP stars led to the classification of carbon-enhanced metal-poor (CEMP) stars, originally based on $[\text{C}/\text{Fe}] > +1.0$ by Beers & Christlieb (2005), but later revised to $[\text{C}/\text{Fe}] > +0.7$ by several authors, which we employ throughout this paper.

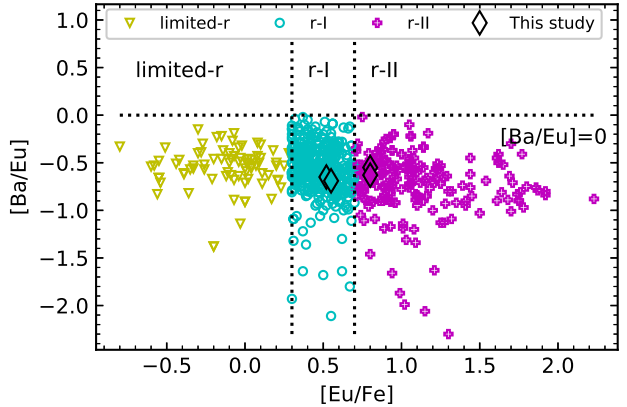
For the classification of our program stars, we first determined

Table 8. Classification of neutron-capture enhanced metal-poor stars.

	Beers & Christlieb (2005)	Cain et al. (2020)	Holmbeck et al. (2020)
r-I	$0.3 \leq [\text{Eu}/\text{Fe}] \leq +1.0$ and $[\text{Ba}/\text{Eu}] < 0$	$0.3 \leq [\text{Eu}/\text{Fe}] \leq +1.0$ and $[\text{Ba}/\text{Eu}] < 0$	$0.3 < [\text{Eu}/\text{Fe}] \leq +0.7$ and $[\text{Ba}/\text{Eu}] < 0$
r-II	$[\text{Eu}/\text{Fe}] > +1.0$ and $[\text{Ba}/\text{Eu}] < 0$	$1.0 < [\text{Eu}/\text{Fe}] \leq +2.0$ and $[\text{Ba}/\text{Eu}] < 0$	$[\text{Eu}/\text{Fe}] > +0.7$ and $[\text{Ba}/\text{Eu}] < 0$
r-III	–	$[\text{Eu}/\text{Fe}] > +2.0$ and $[\text{Ba}/\text{Eu}] < 0$	–
s	$[\text{Ba}/\text{Fe}] > +1.0$ and $[\text{Ba}/\text{Eu}] > +0.5$	–	–
r/s	$0.0 < [\text{Ba}/\text{Eu}] < +0.5$	–	–
limited-r	–	–	$[\text{Eu}/\text{Fe}] < +0.3$, $[\text{Sr}/\text{Ba}] > +0.5$, and $[\text{Sr}/\text{Eu}] > 0.0$

**Figure 10.** Synthesis of regions containing Os and Lu lines. The black dotted points represent the observed spectra and the solid blue colour shows the best fit. The green and red colours indicate ± 0.5 dex deviations from the best fit.

the carbonicity ($[\text{C}/\text{Fe}]$), and find that all of our program stars exhibit $[\text{C}/\text{Fe}] < +0.7$. We then calculated the $[\text{Eu}/\text{Fe}]$ and $[\text{Ba}/\text{Eu}]$ ratios to estimate the level of r -, and s -process enhancement. Fig. 11 shows the location of our program stars in the $[\text{Ba}/\text{Eu}]$ versus $[\text{Eu}/\text{Fe}]$ plane. According to Beers & Christlieb (2005) classification, all of our target stars fall under the r -I category. However, according to the updated classification by Holmbeck et al. (2020), which we use in this study, two stars (HD 263815 and TYC 1191-918-1) are r -I while the other two (TYC 3431-689-1 and TYC 1716-1548-1) are considered as r -II (see Fig. 11).

**Figure 11.** Distribution of $[\text{Ba}/\text{Eu}]$ as a function of $[\text{Eu}/\text{Fe}]$. The limited- r stars are shown in yellow colours, the r -I stars in cyan colours, and the r -II stars in magenta colours. The four black diamonds indicate the r -I (cyan) and r -II (magenta) program stars in this study. References for the compiled data (including from the RPA): McWilliam et al. (1995); Ryan et al. (1996); Burris et al. (2000); Fulbright (2000); Westin et al. (2000); Cowan et al. (2002); Cayrel et al. (2004); Christlieb et al. (2004); Honda et al. (2004); Aoki et al. (2005); Barklem et al. (2005); Ivans et al. (2006); Preston et al. (2006); Lai et al. (2008); Hayek et al. (2009); Aoki et al. (2010); Roederer et al. (2010b); Cohen et al. (2013); Johnson et al. (2013); Hansen et al. (2012); Ishigaki et al. (2013); Mashonkina et al. (2014); Roederer et al. (2014c); Jacobson et al. (2015); Howes et al. (2015); Li et al. (2015a); Hansen et al. (2015a); Howes et al. (2016); Placco et al. (2017); Abohalima & Frebel (2018); Cain et al. (2018); Frebel (2018b); Hansen et al. (2018b); Hawkins & Wyse (2018); Holmbeck et al. (2018); Roederer et al. (2018); Sakari et al. (2018b); Mardini et al. (2019); Valentini et al. (2019); Xing et al. (2019); Cain et al. (2020); Holmbeck et al. (2020); Placco et al. (2020); Rasmussen et al. (2020).

6.2 The Light Elements ($Z < 30$)

Fig. 12 shows the abundances of all the light elements up to Zn for our program stars, along with the data collected from the literature. Our program stars fall on the lower $[\text{C}/\text{Fe}]$ side, which is expected for their current evolutionary stage. Some of the r -II stars in the literature (Abohalima & Frebel 2018) exhibit higher carbonicity ($[\text{C}/\text{Fe}] > +0.7$), which means those stars should fall into the CEMP- r or CEMP- r/s sub-class. We have not considered those stars in this study.

The mixed and unmixed stars are well-separated based on the C and N abundances, as shown in Fig. 13. Nearly two-thirds of the r -II stars fall in the unmixed region, defined with $[\text{N}/\text{Fe}] < +0.5$ (see Spite et al. 2005; Siqueira Mello et al. 2014). Hence, if the C and N abundances are from the natal cloud in which these stars formed, one would expect the presence of lithium in their atmospheres, which can help understand the amount of r -process ejecta mixed

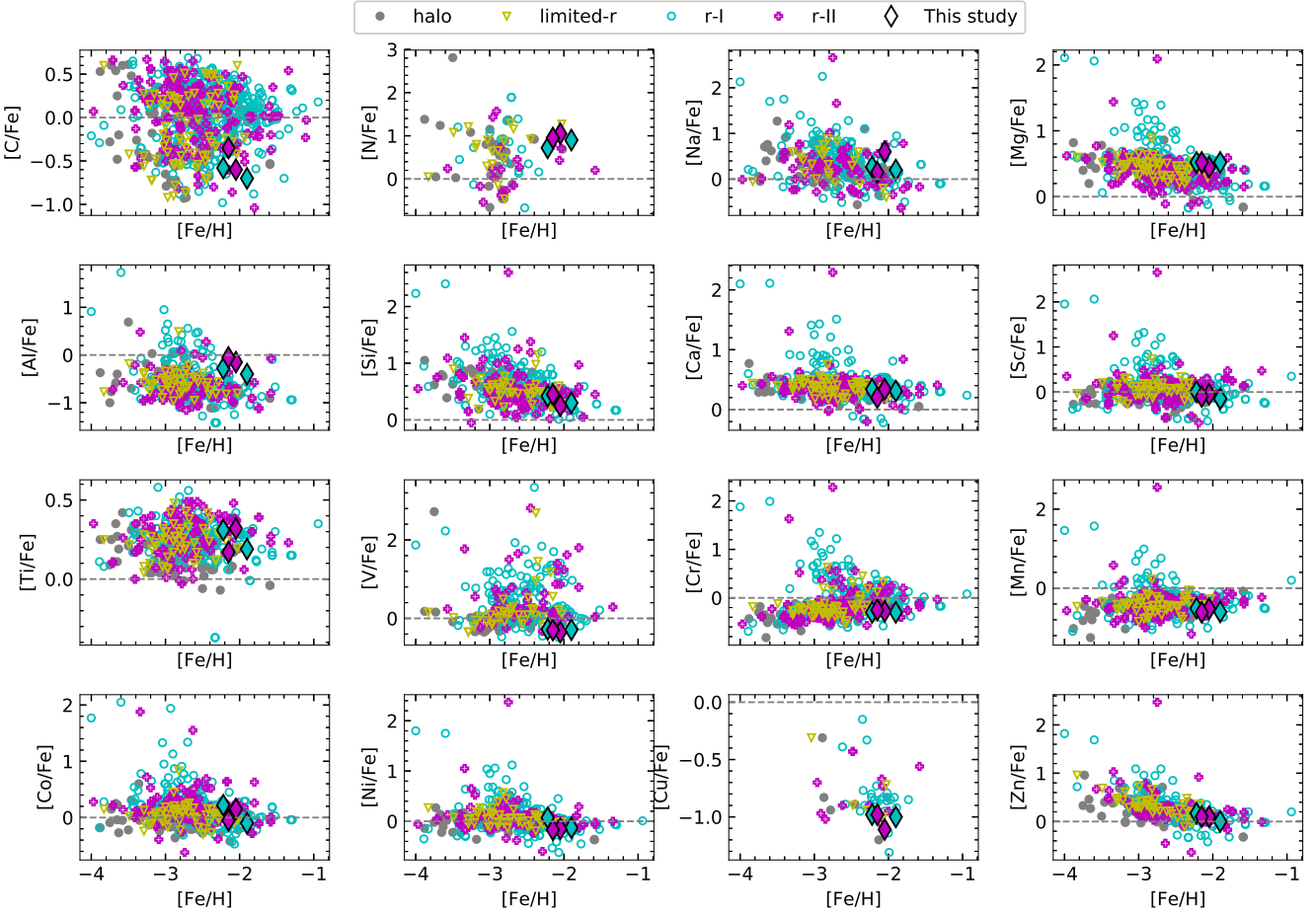


Figure 12. Abundances of the light elements as a function of metallicity. The limited-*r* stars are shown in yellow colours, the *r*-I stars in cyan colours, and the *r*-II stars in magenta colours. The four black diamonds indicate the *r*-I (cyan) and *r*-II (magenta) program stars in this study. References for the *r*-process stars are given in the caption of Fig. 11. Normal metal-poor halo stars, indicated with grey filled circles, are taken from Suda et al. (2008); Ryan et al. (1991); McWilliam et al. (1995); Burris et al. (2000); Fulbright (2000); Aoki et al. (2002); Johnson (2002a); Cayrel et al. (2004); Honda et al. (2004); Aoki et al. (2005); Barklem et al. (2005); Jonsell et al. (2005); Preston et al. (2006); Lai et al. (2007); Zhang et al. (2009); Ishigaki et al. (2010); Roederer et al. (2010a); Hollek et al. (2011); Allen et al. (2012); Aoki et al. (2013a); Cohen et al. (2013); Ishigaki et al. (2013); Yong et al. (2013); Placco et al. (2014a); Roederer et al. (2014a); Hansen et al. (2015b); Jacobson et al. (2015); Li et al. (2015b), and Abohalima & Frebel (2018). The grey horizontal lines represent the solar values.

with the primordial cloud. Four of our program stars exhibit very low [C/N] (< -1.0); they have likely undergone mixing processes. They also show $^{12}\text{C}/^{13}\text{C} < 10$, which further supports mixing in the surface composition. The $^{12}\text{C}/^{13}\text{C}$ values in our program stars are very close to the theoretically predicted CN cycle equilibrium value (Caughlan 1965; Sneden et al. 1986), which is consistent with the position of our target stars in Fig. 13. Similar values of $^{12}\text{C}/^{13}\text{C}$ have been reported in other stars such as HD 122563 (Lambert & Sneden 1977).

Among the odd- Z elements, [Na/Fe] is slightly higher than the solar ratio for our program stars and [Al/Fe] is slightly sub-solar. These values are in good agreement with the known RPE stars. The Na and Al abundances in *r*-I and *r*-II stars exhibit a larger scatter compared to the normal halo stars. The enhanced N abundance along with Na could also indicate a very massive star progenitor for RPE stars. No Na-Mg anti-correlation is apparent.

Halo stars usually exhibit a nearly constant enhancement in the abundance of α -elements ($[\alpha/\text{Fe}] \sim +0.4$). This level of enhancement in the stars comes from core-collapse supernovae. We found $[\alpha/\text{Fe}] = +0.35$ for TYC 3431-689-1, $[\alpha/\text{Fe}] = +0.35$ for

HD 263815, $[\alpha/\text{Fe}] = +0.43$ for TYC 1716-1548-1, and $[\alpha/\text{Fe}] = +0.39$ for TYC 1191-918-1, consistent with the observed values for metal-poor halo stars (McWilliam 1997).

To understand the connection between the α -elements and *r*-process elements, Fig. 14 shows the average α -enhancement, i.e., $\frac{1}{4}([\text{Mg}/\text{Fe}] + [\text{Si}/\text{Fe}] + [\text{Ca}/\text{Fe}] + [\text{Ti}/\text{Fe}])$ for the RPE stars, as a function of $[\text{Eu}/\text{Fe}]$. In this figure, the black solid line shows the best fit after removing the 1σ outliers denoted by overlaid crosses; the shaded region shows the dispersion around the best-fit line. There is only a very weak, statistically insignificant, negative correlation. Our program stars nicely fall on the best-fit line.

The iron-peak elements Sc, Co, and Zn exhibit nearly solar ratios for our program stars, whereas V, Cr, Mn, and Cu fall in the sub-solar region. Abundances of all the iron-peak elements in RPE stars are in good agreement with normal metal-poor halo stars. On average, the halo stars show slightly sub-solar V abundances with a small dispersion, however, RPE stars exhibit significantly higher dispersions towards super-solar abundances. We find that the inclusion of the RPA data from Sakari et al. (2018b) and Ezzeddine et al. (2020) results in a higher dispersion in the [V/Fe] ratio, ranging from

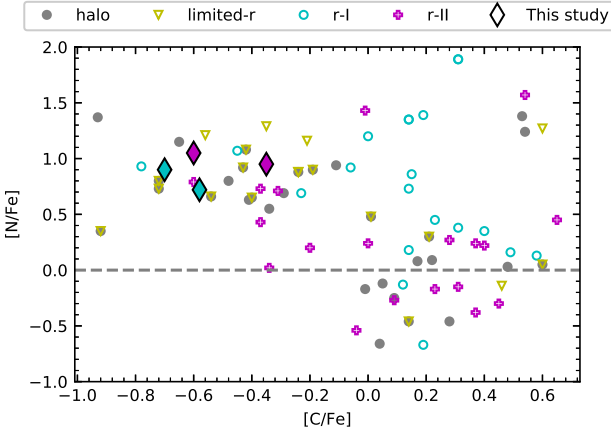


Figure 13. Relation between the N and C abundances. The limited-*r* stars are shown in yellow colours, the *r*-I stars in cyan colours, and the *r*-II stars in magenta colours. The four black diamonds indicate the *r*-I (cyan) and *r*-II (magenta) program stars in this study. References for the RPE stars are given in the caption of Fig. 11, and references for the normal metal-poor halo stars, indicated with grey filled circles, are listed in the caption of Fig. 12. The grey horizontal line represents the solar value.

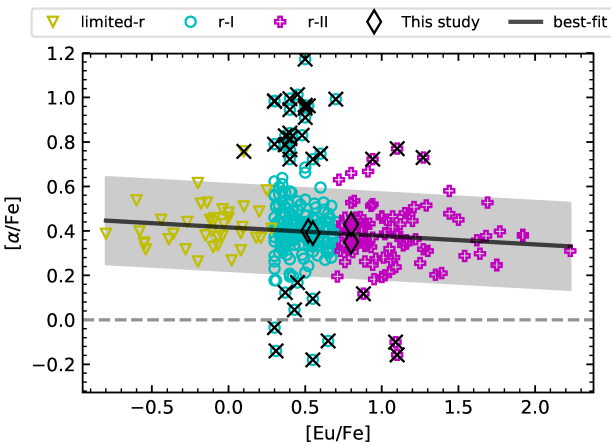


Figure 14. Alpha-element enhancements for RPE stars. The limited-*r* stars are shown in yellow colours, the *r*-I stars in cyan colours, and the *r*-II stars in magenta colours. The four black diamonds indicate the *r*-I (cyan) and *r*-II (magenta) program stars in this study. References for the RPE stars are given in the caption of Fig. 11. The black line is the best fit after removing the 1σ outliers denoted by overlaid crosses. The grey horizontal line represents the solar value.

–0.8 to +3.3. Otherwise, the [V/Fe] ratio remains in the range from –0.8 to +1.0, consistent with previous studies (Sneden et al. 2016; Ou et al. 2020). The [Zn/Fe] ratio increases towards the metal-poor end for *r*-I and *r*-II stars compared to the normal halo stars, indicating a possible additional contribution of Zn from the *r*-process-production site(s) at the metal-poor end. The [Eu/Zn] ratio also exhibits a value closer to normal halo stars at the metal-poor end, and increases with metallicity (see Fig. 15). This indicates that the metal-poor *r*-process-production sites manufactured Zn as well, and with increasing metallicity the *r*-process progenitors either produced less or no zinc. This is consistent with the recent claim for hypernovae or massive SNe being responsible for *r*-process production at the metal-poor end and NSMs contributing at higher metal-

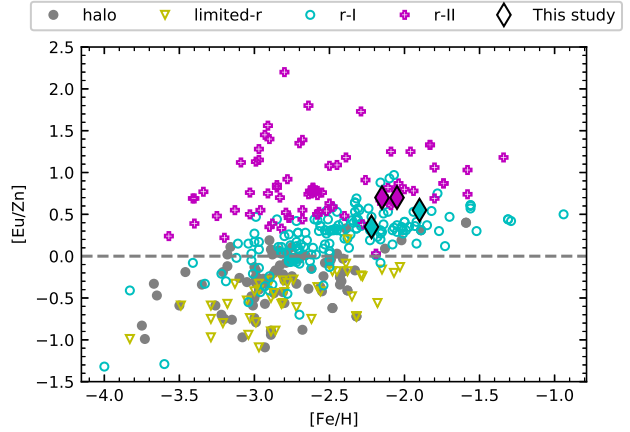


Figure 15. Evolution of the [Eu/Zn] ratio as a function of metallicity. The limited-*r* stars are shown with yellow downward triangles, *r*-I stars are displayed with open cyan circles, and *r*-II stars are represented by magenta crosses. The four black diamonds indicate the *r*-I (cyan) and *r*-II (magenta) program stars in this study. References for the RPE stars are given in the caption of Fig. 11, and references for normal metal-poor halo stars, indicated by grey filled circles, are listed in the caption of Fig. 12. The grey horizontal line represents the solar value.

lurities (Tarumi et al. 2021; Yong et al. 2021). Four of our program stars show [Fe/H] in the range from –2.22 to –1.90 and exhibit near-solar [Zn/Fe] ratios. Also, the [Eu/Zn] ratio of our program stars lies towards the upper limit of [Eu/Zn] for the normal halo stars. It indicates that our program stars may have originated from gas that was primarily enriched by events occurring during the late evolution of the Galaxy, such as NSMs. The contribution from sites that were active in the early Universe may be negligible.

6.3 Evolution of Heavy-element Abundance Ratios for RPE Stars

The [Sr/Ba] ratio reasonably separates the three sub-classes of RPE stars (see Fig. 16(a)). The limited-*r* stars exhibit the highest [Sr/Ba] ratios, and the *r*-II stars show the lowest [Sr/Ba], whereas the *r*-I stars fall in between. However, some *r*-I and *r*-II stars also exhibit higher [Sr/Ba] over the metallicity span of the limited-*r* stars. At low metallicity, we expect the majority of Ba to have come from *r*-process event(s). If Sr were produced from the same *r*-process event(s), we would expect a flat trend of [Sr/Ba] at low metallicity. However, the dispersion of [Sr/Ba] increases with decreasing metallicity (see Fig. 16(b)), indicating an additional formation site for Sr (Travaglio et al. 2004; Aoki et al. 2013b; Spite et al. 2018).

We have also checked on the Sr ratio with respect to the *r*-process element Eu. The distribution of [Sr/Eu] exhibits a similar behaviour as [Sr/Ba], with higher dispersion at low metallicity. Fig. 16(d, e, and f) also exhibits correlations of [Sr/Fe], [Y/Fe], and [Zr/Fe] with respect to [Eu/Fe]. This suggests that some Sr, Y, and Zr are produced in an *r*-process event that synthesises Eu as well. A flatter trend and more scatter in [Sr/Fe] versus [Eu/Fe] could also imply additional sites for the production of Sr as compared to Eu. The plots of [Y/Fe] and [Zr/Fe] versus [Eu/Fe] indicate clear trends, with much less scatter, as compared to the [Sr/Fe] ratio. This could also mean that the additional site that produces Sr does not produce Y and Zr in significant quantities.

Fig. 16(c) shows [Ba/Eu] as a function of metallicity. This ratio

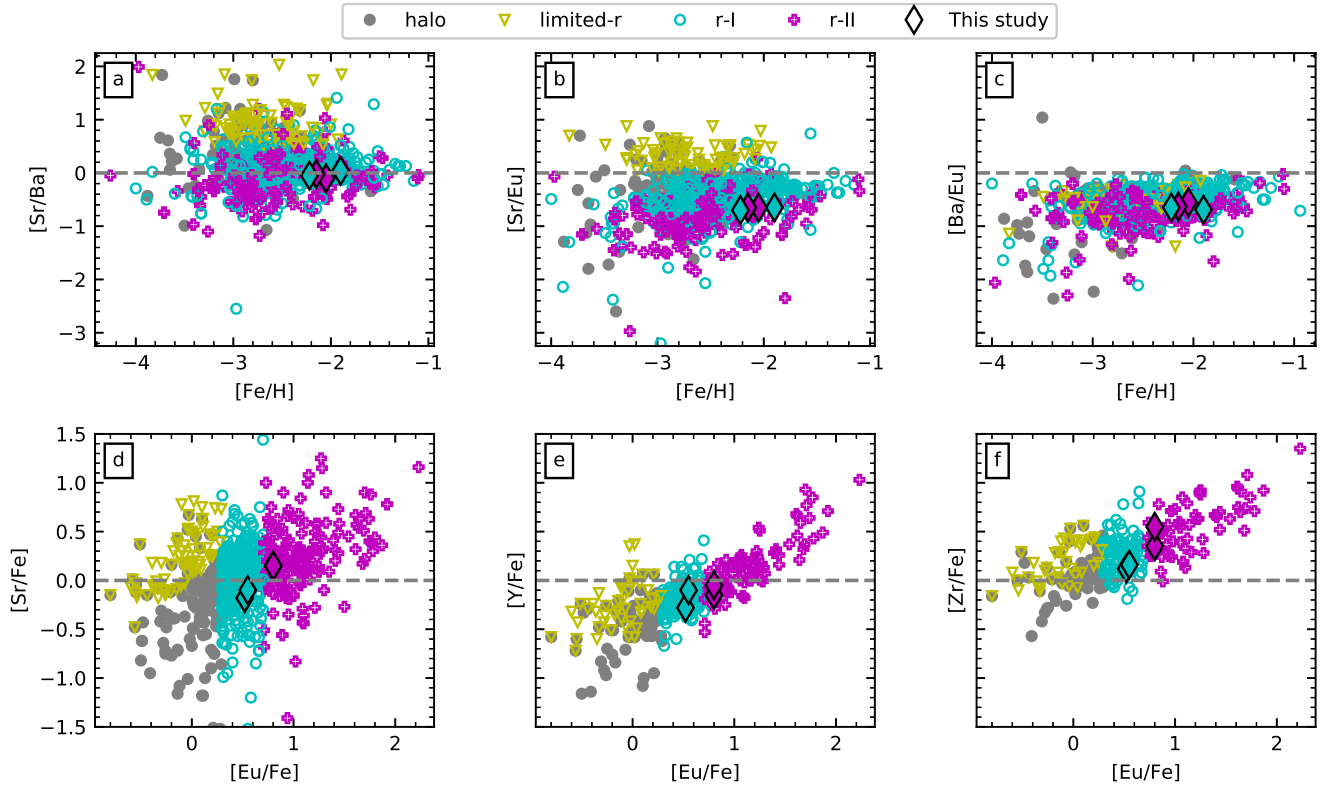


Figure 16. Evolution of neutron-capture abundance ratios as a function of $[{\rm Fe}/{\rm H}]$ and $[{\rm Eu}/{\rm Fe}]$. The limited-*r* stars are shown in yellow colours, the *r*-I stars in cyan colours, and the *r*-II stars in magenta colours. The four black diamonds indicate the *r*-I (cyan) and *r*-II (magenta) program stars in this study. References for the RPE stars are given in the caption of Fig. 11, and references for normal metal-poor halo stars are listed in the caption of Fig. 12.

(excluding a few outliers) exhibits only a small dispersion for the *r*-I, *r*-II and limited-*r* stars, suggesting a similar origin of Ba and Eu in RPE stars. It might be better understood as arising from different levels of dilution of the *r*-process-element yields from the same source.

Four of our program stars exhibit solar $[{\rm Sr}/{{\rm Ba}}]$ ratios. However, the $[{\rm Sr}/{{\rm Eu}}]$ and $[{\rm Ba}/{{\rm Eu}}]$ ratios are sub-solar. For our target stars, $[{\rm Sr}/{{\rm Eu}}]$ ranges from -0.65 to -0.70 and $[{\rm Ba}/{{\rm Eu}}]$ ranges from -0.69 to -0.55 , indicating very little *s*-process contamination. The higher $[{\rm Sr}/{{\rm Ba}}]$ ratio in our program stars as compared to $[{\rm Sr}/{{\rm Eu}}]$ and $[{\rm Ba}/{{\rm Eu}}]$ implies that the interstellar medium (ISM) where these objects were formed was already enriched with the events that produce first *r*-process peak elements and the main *r*-process elements.

Using the literature sample of RPE stars, we find that the limited-*r* stars are poor in C, Fe, and Ba as compared to the *r*-I and *r*-II stars; see Fig. D2(a, b, and d). However, the Sr abundance of the limited-*r* stars spans a similar range as that of the *r*-I and *r*-II stars. All the limited-*r* stars exhibit metallicities lower than $[{\rm Fe}/{\rm H}] = -2.0$, consistent with previous findings (Hansen et al. 2018b; Sakari et al. 2018b). Only one star, 2MASS J14435196-2106283 from Holmbeck et al. (2020), is found at $[{\rm Fe}/{\rm H}] = -1.93$. Also, the $[{\rm C/H}]$ and $[{\rm Ba/H}]$ abundance ratios in limited-*r* stars are always smaller than -2.0 . The evolution-corrected C abundance for all the limited-*r* stars falls in the $[{\rm C/H}] < -1.7$ range. The C and N abundances also indicate that the majority of limited-*r* stars are in the mixed region, indicating that mixing of CN-processed material during their current RGB phase has taken place (see, Fig. 13). Mass transfer from an AGB companion that has gone through the 2nd

dredge-up phase can also result in low carbon abundances. The data on C and N abundances are limited, and we cannot rule out that the $[{\rm C/N}]$ ratio is a result of RGB mixing or due to massive-star wind ejecta. Lithium abundances, along with CN abundances, will provide valuable insights on in-situ/binary origin and an alternative primordial cloud mixed with low-carbon ejecta. These conclusions are based on 46 limited-*r*, 314 *r*-I, and 128 *r*-II stars taken from Gudin et al. (2021). The number of limited-*r* stars is still not sufficiently large to comment further on their nature.

6.4 Production Sites of the Rhird *r*-process Peak

Thorium is purely produced in *r*-process nucleosynthesis. To understand the evolution of Th with other light and heavy elements, we have shown various elemental ratios in Fig. 17. The $[{\rm Th/H}]$ ratio increases with increasing metallicity for both *r*-I and *r*-II stars, as can be seen in 17(a). At a given metallicity, the Th abundance in *r*-II stars is higher than for the *r*-I stars, as evident from 17(a and b). In contrast to $[{\rm Th/H}]$, the $[{\rm Th/Fe}]$ ratio decreases with metallicity, even among *r*-II stars. This could indicate that Fe-peak elements are enriched at a faster rate than the relatively slow radioactive decay of Th.

Fig. 17(c) shows an increasing $[{\rm Eu/Th}]$ ratio with $[{\rm Fe/H}]$. Both *r*-I and *r*-II stars overlap with each other with small scatter. Equal $[{\rm Eu/Th}]$ ratios in *r*-I and *r*-II stars can be explained with the same production sites for both and more dilution of *r*-process ejecta in *r*-I stars.

The $[{\rm Mg/Th}]$ ratio, as a function of $[{\rm Fe/H}]$, in Fig. 17(d) shows

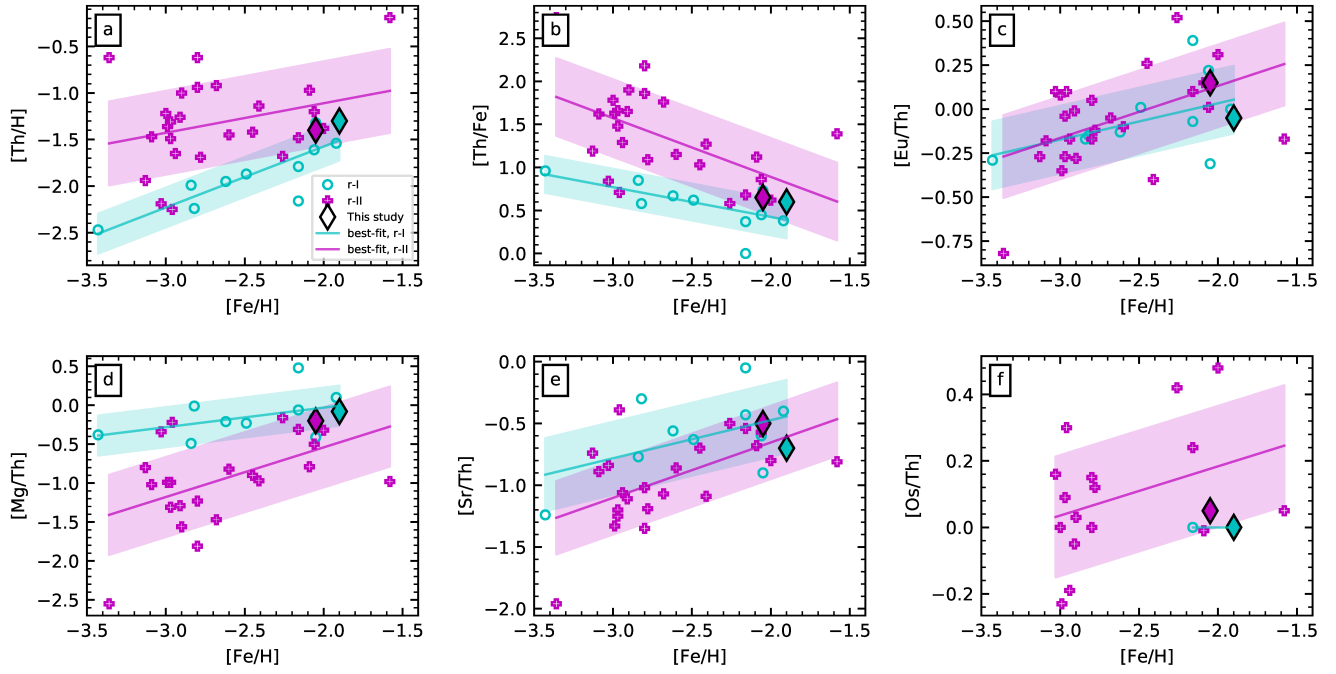


Figure 17. Evolution of ratios of Th with the light and heavy *r*-process elements as a function of metallicity. The *r*-I stars are displayed with open cyan circles, and *r*-II stars are represented by magenta crosses. The four black diamonds indicate the *r*-I (cyan) and *r*-II (magenta) program stars in this study. The cyan and magenta lines represent the best fits to the *r*-I and *r*-II stars, respectively. Their corresponding dispersions are shown with the shaded regions. We have compiled Th abundances from Westin et al. (2000); Cowan et al. (2002); Johnson (2002b); Honda et al. (2004); Ivans et al. (2006); Aoki et al. (2005, 2007); Hayek et al. (2009); Mashonkina et al. (2010, 2014); Roederer et al. (2014b,c); Siqueira Mello et al. (2014); Hill et al. (2017); Placco et al. (2017); Holmbeck et al. (2018); Sakari et al. (2018a)

interesting distributions of *r*-I and *r*-II stars. All the *r*-I stars have higher [Mg/Th] ratios than the *r*-II stars. With increasing metallicity, [Mg/Th] appears to converge to zero, where *r*-II stars have steeper slope than *r*-I stars. These trends indicate that, apart from the difference in the level of mixing of the *r*-process ejecta in the inherited composition of *r*-I and *r*-II stars, the *r*-II stars could have formed earlier than *r*-I stars. Fig. 17(e) shows the [Sr/Th] evolution with [Fe/H]. It exhibits similar trends for *r*-I and *r*-II stars as that of [Eu/Th], but with larger dispersion. Finally, we have plotted the third-peak element [Os/Th] ratio with metallicity in Fig. 17(f). For *r*-II stars, it shows that the [Os/Th] ratio increases with metallicity, similar to the [Eu/Th] ratio. We have only two *r*-I stars with detected Os and Th, thus we cannot comment about their evolution. In the future, a larger number of RPE stars with detected Os and Th abundances should help reveal more about their evolution.

Two of our program stars with measured Th are at the larger [Fe/H] values of the sample. Also, both of them lying in the overlapping region of *r*-I and *r*-II trends, as can be seen in all the panels of Fig. 17. The separation of *r*-I and *r*-II sub-classes at the lower-metallicity end seems to disappear as we observe Th evolution with other elements from lighter to heavier elements. Being in overlapping regions and towards the larger [Fe/H] side indicates that our program stars are primarily enriched by single main *r*-process events, such as NSMs, with little contribution from a limited-*r* process event.

6.5 The *r*-process pattern

The abundances of the elements produced in the *r*-process, as a function of their atomic numbers, exhibit a distinctive pattern known

as the *r*-process pattern. This pattern shows three noticeable peaks, at atomic number $Z \sim 35$ (first peak: best probed with Sr, Y, and Zr), $Z \sim 54$ (second peak: best probed with Ba and La), and $Z \sim 78$ (third peak: best probed with Os and Ir). These peaks are the result of three closed neutron shells with neutron numbers 50, 82, and 126, respectively (Sneden et al. 2008; Ji & Frebel 2018).

Numerous previous studies found that the abundance patterns of metal-poor RPE stars match very closely with the scaled-solar *r*-process pattern (Sneden et al. 1998; Sneden et al. 2008). This agreement is more pronounced for lanthanides, the elements from Ba to Hf. Lighter *r*-process elements exhibit scatter from the scaled-solar *r*-process pattern, which is attributed to the result of a different formation mechanism, called the weak *r*-process or limited-*r* process. The scatter of the actinide elements was expected due to their radioactive nature. However, some stars exhibit Th in excess amounts as compared to the scaled-solar *r*-process pattern. These stars are known as actinide-boost stars (Schatz et al. 2002; Mashonkina et al. 2014).

The top panel of Fig. 18 shows the abundance distribution of our program stars, as a function of their atomic number, scaled to the solar *r*-process pattern with respect to Eu. The bottom panel displays the residual abundances of the stars from the scaled-solar *r*-process pattern. The *r*-process-element abundances of our program stars also match with the scaled-solar *r*-process abundances, confirming the universality of the main *r*-process pattern (second-peak elements), along with the usual scatter for the first and third *r*-process elements.

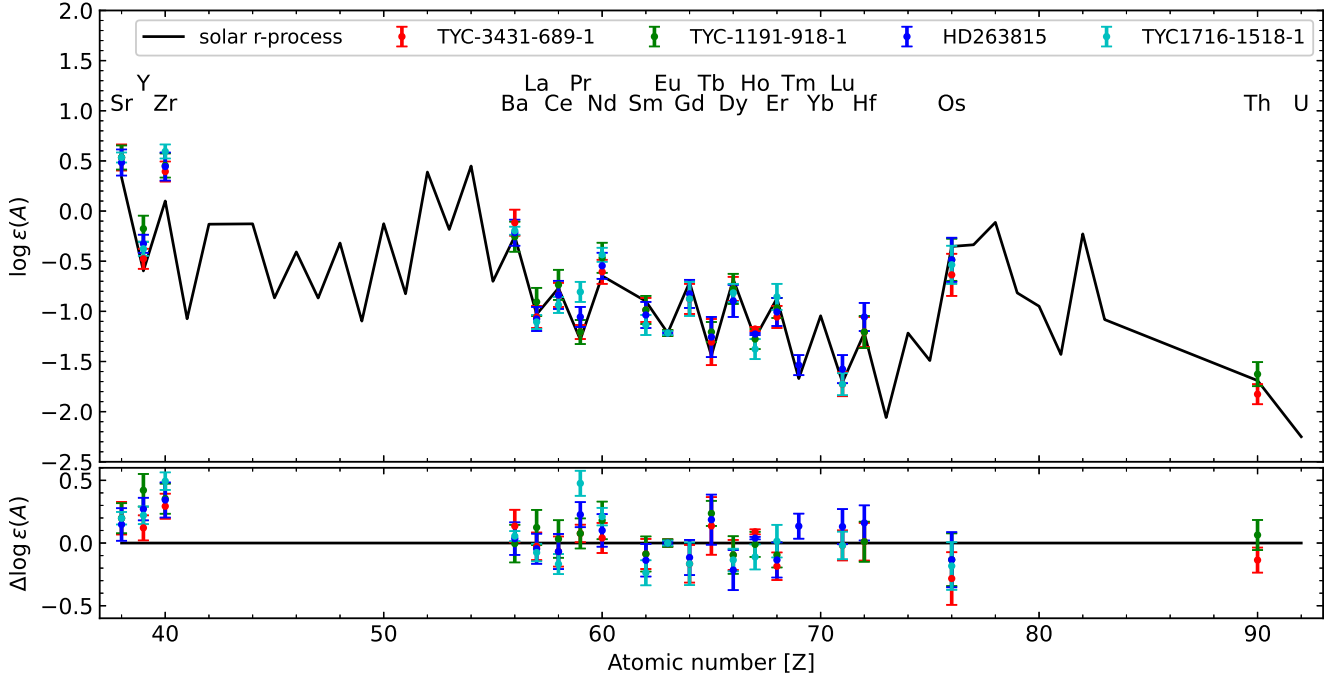


Figure 18. Top panel: The solid black line shows the solar *r*-process pattern, i.e., the absolute abundance ($\log \epsilon$) as a function of atomic number (Z). The elemental abundances of our program stars are scaled to the solar Eu abundance. Bottom panel: Residual abundances of our program stars are calculated as the difference of scaled stellar abundance and the solar abundance. The solar *r*-process pattern is adopted from Arlandini et al. (1999).

6.6 Effect of $\log g f$ Values on Actinide Classification and Age estimation

Among all of the actinide elements, we could only make estimates of the Th abundance for two of our program stars, TYC 1191-918-1 (*r*-I star) and TYC 3431-689-1 (*r*-II star). We have calculated an upper limit for a third star, HD 263815. Thorium is a radioactive element with a half-life of 14.05 Gyr. The production of Th is only possible in *r*-process nucleosynthesis (Cowan et al. 1991).

There has been noticed a quite significant dispersion in the actinide-to-lanthanide abundance ratios among metal-poor stars (see Holmbeck et al. 2018 and references therein). Generally, $\log \epsilon(\text{Th}/\text{Eu})$ is used as an indicator to measure the actinide-to-lanthanide abundance ratio. Around 30% of RPE stars exhibit a 2 to 3 times higher Th/Eu ratio as compared to other RPE stars (Hill et al. 2002; Mashonkina et al. 2014). These stars, with $\log \epsilon(\text{Th}/\text{Eu}) > -0.5 \pm 0.15$, are known as actinide-boost stars (Holmbeck et al. 2018). Recently, Holmbeck et al. (2019) used $\log \epsilon(\text{Th}/\text{Dy})$ to classify stars in different actinide categories as follows:

$$\begin{aligned} \text{actinide-deficient: } & \log \epsilon(\text{Th}/\text{Dy}) < -1.20 \\ \text{actinide-normal: } & -1.20 \leq \log \epsilon(\text{Th}/\text{Dy}) \leq -0.90 \\ \text{actinide-boost: } & \log \epsilon(\text{Th}/\text{Dy}) > -0.90 \end{aligned}$$

The radioactive nature of Th is often used as chronometer to estimate stellar ages (more precisely, the time elapsed since its production, hence a lower limit on the stellar age). The thorium chronometer is based on the universality of the *r*-process pattern. The depletion of Th with respect to non-radioactive elements heavier than Ba, such as Ce, Eu, Dy, Os, Ir, etc., are used for stellar age calculation. The age of a star can be estimated using the following

relation (Cayrel et al. 2001; Cain et al. 2018; Hansen et al. 2018a):

$$\Delta t = 46.7 [\log \epsilon(\text{Th}/X)_i - \log \epsilon(\text{Th}/X)_f], \quad (1)$$

where X is a non-radioactive element above Ba, $\log \epsilon(\text{Th}/X)_i$ is the initial abundance ratio at the time of star's birth, also known as the production ratio (PR), and $\log \epsilon(\text{Th}/X)_f$ is the final abundance ratio, i.e., now. The error in age is calculated from:

$$\Delta t_{\text{err}} = 46.7 \sqrt{\sigma_{\log \epsilon(\text{Th})}^2 + \sigma_{\log \epsilon(X)}^2}, \quad (2)$$

where $\sigma_{\log \epsilon(\text{Th})}$ and $\sigma_{\log \epsilon(X)}$ are the errors in the abundance of Th and element X, respectively. Since the age determination depends only on this abundance ratio, it is necessary to precisely estimate the Th abundance – a small error of 0.2 dex in $\log(\text{Th}/\text{Eu})$ can produce a 9.3 Gyr error in the age estimate.

Even if we carefully consider effects of the blending in the abundance estimation of Th, the choice of $\log g f$ can significantly affect its abundance determination. In the literature, the value of $\log g f$ for this species is continuously being updated; the current value of $\log g f$ may differ from previously employed values, resulting in different abundance estimates. For example, Fig. 19 compares the spectrum synthesis of the Th II line at 4019 Å in TYC 1191-918-1 for two different $\log g f$ values, -0.228 and -0.651. Here, the dotted line corresponds to the observed spectrum and the solid blue line is the best fit, while the green and red lines correspond to 0.5 dex deviations from the best fit. As expected, different $\log g f$ values yield different Th abundances, leading to significant errors in the age estimation of the star. We adopt an updated value of $\log g f = -0.228$ for Th abundance estimation, and use the resulting abundance for the age calculation of our program stars. The PR of elements in equation (1) is taken from Schatz et al. (2002) and Hill et al. (2017). Estimated ages from individual species and their medians for Th-detected stars are listed in Tables 9 and 10. Follow-

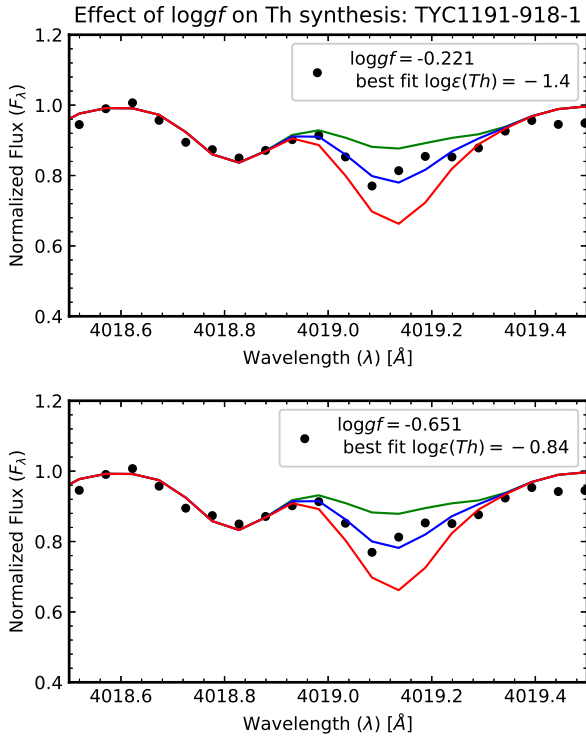


Figure 19. Synthesis of the Th II 4019 Å region in TYC 1191-918-1 for two different values of $\log g f$, -0.221 and -0.651 . The dotted line represents the observed spectrum and the solid blue line is the best-fit synthetic spectrum. The green and red lines show 0.5 dex deviations from the best-fit line.

ing recent PR values from (Hill et al. 2017), the median age of TYC 3431-689-1 is 14.36 ± 7.3 Gyr, which can be expected for a VMP star. However, the median age of TYC 1191-918-1 is 9.19 ± 8.98 Gyr, which is lower than expected, due to the higher Th abundance.

Th and U are the most useful elements for estimating ages for ~ 10 Gyr-old stars. The primary sources of uncertainty in the Th chronometer are its long half-life of 14.05 Gyr and production ratio of the second and third *r*-process peak elements. The detection of U along with Th would have been of much importance to constrain the ages of our program stars independent from stellar evolution models, and thus the minimum age of the Universe because U has a smaller half-life of 4.5 Gyr, both the elements (Th and U) belongs to same (third) *r*-process peak, and are only produced in *r*-process nucleosynthesis (see, Cayrel et al. 2001; Barbuy et al. 2011).

We have also calculated the actinide-to-lanthanide abundance ratio for our program stars with detected Th. Following Holmbeck et al. (2018), both of our program stars with Th belong to the actinide-normal category. On the other hand, according to the Holmbeck et al. (2019) criterion, TYC 3431-689-1 again falls in the actinide-normal class, whereas TYC 1191-918-1 moves into the actinide-boost region, close to the separation boundary. We believe this determination of an actinide boost may be due to the uncertainties in our abundance estimation. TYC 1191-918-1 was earlier reported to be an actinide-boost star by Bandyopadhyay et al. (2020b), with $\log \epsilon(\text{Th/Eu}) = -0.20$. There could be three possible reasons for their higher actinide-to-lanthanide ratio: (1) differences in the adopted stellar parameters, (2) incomplete accounting of the contribution from blended elements, and/or (3) their choice of a lower $\log g f$ value.

Fig. 20 shows $\log \epsilon(\text{Th/Eu})$, as a function of $[\text{Fe/H}]$, for our

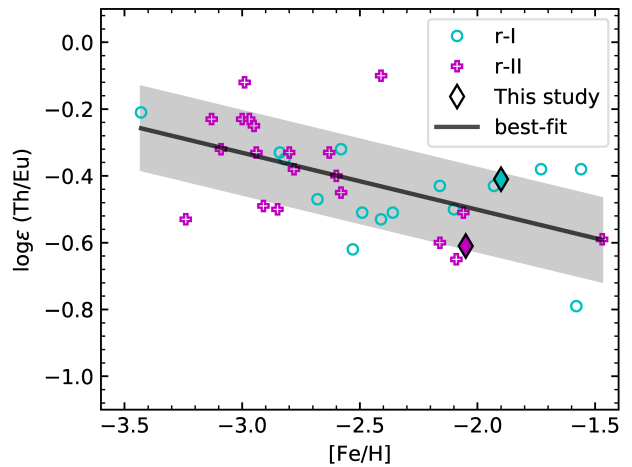


Figure 20. The $\log \epsilon(\text{Th/Eu})$ value, as a function of metallicity, for RPE stars with measured Th. The *r*-I stars are shown with cyan-coloured open circles and the *r*-II stars with magenta-coloured crosses. The black diamonds indicate the *r*-I (cyan) and *r*-II (magenta) program stars in this study. The black line represents the best fit to the data and the shaded region shows its dispersion. The references for stars with detected Th are given in the caption of Fig. 17.

two Th-detected stars, overlaid with RPE stars from the literature. Our program stars are shown with black diamonds, whereas *r*-I and *r*-II stars are represented by cyan circles and magenta crosses, respectively. The black solid line represents the best-fit linear relationship, and the grey colour region shows the dispersion around the best-fit line. From inspection, there is a clear trend of a decreasing actinide-to-lanthanide ratio with increasing metallicity. If we take metallicity as a proxy for age, this implies that older stars are more actinide rich than younger stars, contrary to the universality of the *r*-process pattern. According to this paradigm, older stars should be more actinide poor than the younger stars. This opposite trend could be the result of two possibilities for non-universal production ratio: (1) the late universe is enriched by lanthanides or (2) the early universe is enriched by actinides. The first possibility appears more likely in terms of the production site(s) of these elements, although the production sites of the actinides are less-well understood.

The assumption of a linear trend of the actinide-to-lanthanide production ratio with metallicity may be one of the possible reasons for higher dispersion in this ratio, leading to the actinide-boost phenomenon. Assuming a constant actinide-to-lanthanide production ratio yields negative ages for actinide-boost stars and large uncertainties in the age estimation using this method. If the *r*-process pattern is truly universal, the production ratio needs to be calibrated for the chemical evolution of the Galaxy. And of course, a much larger sample of RPE stars is needed to provide better constraints on the astrophysical formation sites of such stars.

7 CONCLUSIONS

In this study, we estimate a more complete set of elemental abundances for four relatively bright ($V < 12$) VMP RPE stars observed with the 10-m class GTC telescope. Due to the excellent SNR of the spectra in the blue region, we could estimate the abundances of ten neutron-capture elements for these stars that were not reported by Bandyopadhyay et al. (2020b): Pr, Gd, Tb, Ho, Hf, Er, Tm, Lu, Os, and Th, and improved estimates for others. We find that two

Table 9. Age estimation of TYC 3431-689-1.

<i>Th/X</i>	PR (Schatz et al. 2002)	TYC 3431-689-1 Age (Gyr)	PR (Hill et al. 2017)	Age (Gyr)	σ (Gyr)
Th/Ba	–	–	–1.058	30.50	7.67
Th/La	–0.60	7.95	–0.362	19.08	6.95
Th/Ce	–0.79	9.35	–0.724	12.44	7.30
Th/Pr	–0.30	14.96	–0.313	14.36	5.71
Th/Nd	–0.91	14.50	–0.928	13.65	7.30
Th/Sm	–0.61	10.75	–0.796	2.05	7.30
Th/Eu	–0.33	13.09	–0.240	17.3	4.88
Th/Gd	–0.81	6.54	–0.569	17.8	8.43
Th/Dy	–0.89	7.48	–0.827	10.43	7.30
Th/Ho	–	–	–0.071	27.08	4.77
Th/Er	–0.68	4.21	–0.592	8.32	6.95
Th/Hf	–0.20	19.64	–0.036	27.31	8.4
Th/Os	–1.15	1.87	–0.917	12.77	10.88
Median		9.35		14.36	7.30

Table 10. Age estimation of TYC 1191-918-1.

<i>Th/X</i>	PR (Schatz et al. 2002)	TYC 1191-918-1 Age (Gyr)	PR (Hill et al. 2017)	Age (Gyr)	σ (Gyr)
Th/Ba	–	–	–1.058	14.59	8.98
Th/La	–0.60	5.61	–0.362	16.74	8.62
Th/Ce	–0.79	4.67	–0.724	7.76	8.98
Th/Pr	–0.30	5.61	–0.313	5.00	7.93
Th/Nd	–0.91	11.69	–0.928	10.85	8.98
Th/Sm	–0.61	1.40	–0.796	–7.29	8.62
Th/Eu	–0.33	3.74	–0.240	7.95	5.78
Th/Gd	–0.81	–	–0.569	–	–
Th/Dy	–0.89	–1.87	–0.827	1.07	8.98
Th/Ho	–	–	–0.071	–	–
Th/Er	–0.68	–	–0.592	–	–
Th/Hf	–0.20	10.29	–0.036	17.96	9.35
Th/Os	–1.15	–0.467	–0.917	10.43	11.31
Median		4.67		9.19	8.98

of our targets fall under the *r*-I classification, while the other two are *r*-II stars. We could measure Th in TYC 1191-918-1 (*r*-I star) and TYC 3431-689-1 (*r*-II star). In our study, we also obtain upper limits of for the Pb abundances of HD 263815, TYC 3431-689-1, and TYC 1716-1548-1. The elemental-abundance patterns of our stars are well-matched with the scaled-solar *r*-process patterns in the main *r*-process region (Ba to Hf). We find [C/N] < –1.0 and $^{12}\text{C}/^{13}\text{C} < 10$, which indicates internal mixing of CN-cycle nucleosynthesis products altering the surface composition.

We also study the elemental-abundance trends among the RPE stars; the main conclusions are listed below.

- The RPE stars exhibit a similar trend in $[\alpha/\text{Fe}]$ and $[\text{Fe}/\text{H}]$ as compared to the normal metal-poor halo stars. However, *r*-II stars exhibit a declining trend with respect to $[\text{Eu}/\text{Fe}]$, which may indicate efficient mixing of the ISM at higher metallicities. Four of our program stars also follow the expected trends of other RPE stars.
- The compiled RPE stars exhibit similar trends in the Fe-peak elements as that of the halo stars, however there is a large scatter noticed in the trends of Sc, V, Cr, especially at low metallicities. A homogeneous analysis might be useful to confirm various trends.

The targets of the current study follow the same trend as that of the other halo stars at the same metallicities. Also, the Fe-peak elements have flat trends with respect to $[\text{Eu}/\text{Fe}]$, excepting Mn, Cr, and Zn. We found that metal-poor stars exhibit high $[\text{Zn}/\text{Fe}]$ and low $[\text{Eu}/\text{Zn}]$, hinting at Zn production with *r*-process events in the early Galaxy. Four of our program stars show $[\text{Fe}/\text{H}]$ in the range from –2.22 to –1.90, and exhibit near-solar $[\text{Zn}/\text{Fe}]$ ratios, suggesting insignificant contribution of Zn from the *r*-process source.

- The $[\text{Sr}/\text{Fe}]$ ratio exhibits a relatively flat trend with respect to $[\text{Eu}/\text{Fe}]$ and large scatter, however $[\text{Y}/\text{Fe}]$ and $[\text{Zr}/\text{Fe}]$ show steeper trends and less scatter with respect to $[\text{Eu}/\text{Fe}]$. This indicates that the site that made Eu is also a significant contributor of Y and Zr as compared to Sr.
- The abundance trend in Th and Mg with respect to $[\text{Fe}/\text{H}]$ indicates that there could be some delay between the formation of *r*-II stars and *r*-I stars.
- Due to the radioactive nature of Th, we could calculate age estimates for TYC 3431-689-1 and TYC 1191-918-1, as 14.36 ± 7.3 and 9.19 ± 8.98 Gyr, respectively. We emphasize the role that production ratios, nuclear physics, and astrophysical sites of the *r*-process play a role on the uncertainty in age estimation.

Some of the interesting signatures we find are suggestive, but firm conclusions require additional data (more stars, more abundances) based on a homogeneous analysis, continuing on the path pioneered by the RPA. Along with the discovery of a larger number of RPE stars, the abundances of many elements across the neutron-capture peaks over a larger metallicity range can help identify the astrophysical sites of the *r*-process and their relative contribution to the chemical history of the Galaxy.

ACKNOWLEDGEMENTS

We thank the anonymous reviewer for valuable comments and suggestions which improved our paper. PS thanks ABSR, AK, and RS for their useful discussions during this study. We thank Vinicius Placco for providing carbon correction values. CAP is thankful for funding from the Spanish government through grants AYA2014-56359-P, AYA2017-86389-P and PID2020-117493GB-I00. TCB acknowledges partial support for this work from grant PHY 14-30152; Physics Frontier Center/JINA Center for the Evolution of the Elements (JINA-CEE), and OISE-1927130: The International Research Network for Nuclear Astrophysics (IReNA), awarded by the US National Science Foundation. This work makes use of data from the European Space Agency (ESA) mission *Gaia* (<https://www.cosmos.esa.int/gaia>), processed by the *Gaia* Data Processing and Analysis Consortium (DPAC, <https://www.cosmos.esa.int/web/gaia/dpac/consortium>). Funding for the DPAC has been provided by national institutions, in particular the institutions participating in the *Gaia* Multilateral Agreement. This work makes use of Astropy:⁵ a community-developed core Python package and an ecosystem of tools and resources for astronomy (Astropy Collaboration et al. 2013, 2018, 2022). This publication makes use of VOSA, developed under the Spanish Virtual Observatory (<https://svo.cab.inta-csic.es>) project funded by MCIN/AEI/10.13039/501100011033/ through grant PID2020-112949GB-I00. This work makes use of Matplotlib (Hunter 2007), NumPy (Harris et al. 2020), and Pandas (Wes McKinney 2010; pandas development team 2020).

DATA AVAILABILITY

The data used in this research will be shared on reasonable request to the corresponding author.

REFERENCES

- Abohalima A., Frebel A., 2018, *ApJS*, **238**, 36
 Allen D. M., Ryan S. G., Rossi S., Beers T. C., Tsangarides S. A., 2012, *A&A*, **548**, A34
 Allende Prieto C., 2021, *Nature Astronomy*, **5**, 105
 Alonso A., Arribas S., Martínez-Roger C., 1999, *A&AS*, **140**, 261
 Alvarez R., Plez B., 1998, *A&A*, **330**, 1109
 Andrievsky S. M., Spite M., Korotin S. A., Spite F., Bonifacio P., Cayrel R., Hill V., François P., 2007, *A&A*, **464**, 1081
 Andrievsky S. M., Spite M., Korotin S. A., Spite F., Bonifacio P., Cayrel R., Hill V., François P., 2008, *A&A*, **481**, 481
 Aoki W., Norris J. E., Ryan S. G., Beers T. C., Ando H., 2002, *PASJ*, **54**, 933
 Aoki W., et al., 2005, *ApJ*, **632**, 611
 Aoki W., et al., 2007, *ApJ*, **660**, 747
 Aoki W., Beers T. C., Honda S., Carollo D., 2010, *ApJ*, **723**, L201
 Aoki W., et al., 2013a, *AJ*, **145**, 13
 Aoki W., Suda T., Boyd R. N., Kajino T., Famiano M. A., 2013b, *ApJ*, **766**, L13
 Arcavi I., et al., 2017, *Nature*, **551**, 64
 Arcones A., Janka H. T., Scheck L., 2007, *A&A*, **467**, 1227
 Arcoragi J. P., Langer N., Arnould M., 1991, *A&A*, **249**, 134
 Argast D., Samland M., Thielemann F. K., Qian Y. Z., 2004, *A&A*, **416**, 997
 Arlandini C., Käppeler F., Wissak K., Gallino R., Lugardo M., Busso M., Straniero O., 1999, *ApJ*, **525**, 886
 Arnett W. D., Thielemann F. K., 1985, *ApJ*, **295**, 589
 Asplund M., Grevesse N., Sauval A. J., Scott P., 2009, *ARA&A*, **47**, 481
 Astropy Collaboration et al., 2013, *A&A*, **558**, A33
 Astropy Collaboration et al., 2018, *AJ*, **156**, 123
 Astropy Collaboration et al., 2022, *apj*, **935**, 167
 Bandyopadhyay A., Thirupathi S., Beers T. C., Susmitha A., 2020a, *MNRAS*, **494**, 36
 Bandyopadhyay A., Sivarani T., Beers T. C., 2020b, *ApJ*, **899**, 22
 Banerjee P., Wu M.-R., Yuan Z., 2020, *ApJ*, **902**, L34
 Barbuy B., et al., 2011, *A&A*, **534**, A60
 Barklem P. S., O'Mara B. J., 2001, *Journal of Physics B Atomic Molecular Physics*, **34**, 4785
 Barklem P. S., et al., 2005, *A&A*, **439**, 129
 Baumueller D., Gehren T., 1997, *A&A*, **325**, 1088
 Bayo A., Rodrigo C., Barrado Y Navascués D., Solano E., Gutiérrez R., Morales-Calderón M., Allard L., 2008, *A&A*, **492**, 277
 Beers T. C., Christlieb N., 2005, *ARA&A*, **43**, 531
 Bergemann M., Hansen C. J., Bautista M., Ruchti G., 2012, *A&A*, **546**, A90
 Bethe H. A., 1990, *Reviews of Modern Physics*, **62**, 801
 Biémont É., et al., 2011, *MNRAS*, **414**, 3350
 Bisterzo S., Gallino R., Straniero O., Cristallo S., Käppeler F., 2010, *MNRAS*, **404**, 1529
 Bord D. J., Cowley C. R., Mirjianian D., 1997, in American Astronomical Society Meeting Abstracts #190. p. 04.01
 Bovard L., Martin D., Guercilena F., Arcones A., Rezzolla L., Korobkin O., 2017, *Phys. Rev. D*, **96**, 124005
 Bressan A., Marigo P., Girardi L., Salasnich B., Dal Cero C., Rubele S., Nanni A., 2012, *MNRAS*, **427**, 127
 Burbidge E. M., Burbidge G. R., Fowler W. A., Hoyle F., 1957, *Reviews of Modern Physics*, **29**, 547
 Burris D. L., Pilachowski C. A., Armandroff T. E., Sneden C., Cowan J. J., Roe H., 2000, *ApJ*, **544**, 302
 Cain M., et al., 2018, *ApJ*, **864**, 43
 Cain M., et al., 2020, *ApJ*, **898**, 40
 Cameron A. G. W., 1957, *PASP*, **69**, 201
 Campbell S. W., Lattanzio J. C., 2008, *A&A*, **490**, 769
 Cardon B. L., Smith P. L., Scalo J. M., Testerman L., Whaling W., 1982, *ApJ*, **260**, 395
 Castelli F., Kurucz R. L., 2003, in Piskunov N., Weiss W. W., Gray D. F., eds, Proceedings of the International Astronomical Union Vol. 210, Modelling of Stellar Atmospheres. p. A20 ([arXiv:astro-ph/0405087](https://arxiv.org/abs/astro-ph/0405087))
 Caughlan G. R., 1965, *ApJ*, **141**, 688
 Cayrel R., 1988, in Cayrel de Strobel G., Spite M., eds, Proceedings of the International Astronomical Union Vol. 132, The Impact of Very High S/N Spectroscopy on Stellar Physics. p. 345
 Cayrel R., et al., 2001, *Nature*, **409**, 691
 Cayrel R., et al., 2004, *A&A*, **416**, 1117
 Chornock R., et al., 2017, *ApJ*, **848**, L19
 Christlieb N., Gustafsson B., Korn A. J., Barklem P. S., Beers T. C., Bessell M. S., Karlsson T., Mizuno-Wiedner M., 2004, *ApJ*, **603**, 708
 Clayton D. D., 1983, Principles of stellar evolution and nucleosynthesis. Chicago: University of Chicago Press
 Cohen J. G., Christlieb N., Thompson I., McWilliam A., Shectman S., Reimers D., Wisotzki L., Kirby E., 2013, *ApJ*, **778**, 56
 Cowan J. J., Rose W. K., 1977, *ApJ*, **212**, 149
 Cowan J. J., Thielemann F.-K., Truran J. W., 1991, *Phys. Rep.*, **208**, 267
 Cowan J. J., et al., 2002, *ApJ*, **572**, 861
 Cui W. Y., Sivarani T., Christlieb N., 2013, *A&A*, **558**, A36

⁵ <http://www.astropy.org>

- Curtis S., Ebinger K., Fröhlich C., Hempel M., Perego A., Liebendörfer M., Thielemann F.-K., 2019, *ApJ*, **870**, 2
- Den Hartog E. A., Lawler J. E., Sobeck J. S., Sneden C., Cowan J. J., 2011, *ApJS*, **194**, 35
- Denissenkov P. A., Herwig F., Battino U., Ritter C., Pignatari M., Jones S., Paxton B., 2017, *ApJ*, **834**, L10
- Denissenkov P. A., Herwig F., Woodward P., Andrassy R., Pignatari M., Jones S., 2019, *MNRAS*, **488**, 4258
- Doherty C. L., Gil-Pons P., Siess L., Lattanzio J. C., Lau H. H. B., 2015, *MNRAS*, **446**, 2599
- Drout M. R., et al., 2017, *Science*, **358**, 1570
- Ezzeddine R., et al., 2020, *ApJ*, **898**, 150
- Frebel A., 2018a, *Annual Review of Nuclear and Particle Science*, **68**, 237
- Frebel A., 2018b, *Annual Review of Nuclear and Particle Science*, **68**, 237
- Frebel A., Norris J. E., 2015, *ARA&A*, **53**, 631
- Frebel A., et al., 2005, *Nature*, **434**, 871
- Frebel A., Yu Q., Jacobson H. R., 2016, in *Journal of Physics Conference Series*. p. 012051, doi:10.1088/1742-6596/665/1/012051
- Freiburghaus C., Rosswog S., Thielemann F. K., 1999, *ApJ*, **525**, L121
- Fujimoto S.-i., Nishimura N., Hashimoto M.-a., 2008, *ApJ*, **680**, 1350
- Fulbright J. P., 2000, *AJ*, **120**, 1841
- Gaia Collaboration 2022, VizieR Online Data Catalog, p. I/355
- Gaia Collaboration et al., 2021, *A&A*, **649**, A1
- Gallagher A. J., Ryan S. G., Hosford A., García Pérez A. E., Aoki W., Honda S., 2012, *A&A*, **538**, A118
- Ge J., et al., 2015, in *American Astronomical Society Meeting Abstracts* #225. p. 409.03
- Gehren T., Liang Y. C., Shi J. R., Zhang H. W., Zhao G., 2004, *A&A*, **413**, 1045
- Goriely S., Bauswein A., Janka H.-T., 2011, *ApJ*, **738**, L32
- Gudin D., et al., 2021, *ApJ*, **908**, 79
- Hansen C. J., Kawaler S. D., Trimble V., 2004, *Stellar interiors : physical principles, structure, and evolution*. New York: Springer-Verlag
- Hansen C. J., et al., 2012, *A&A*, **545**, A31
- Hansen T., et al., 2015a, *ApJ*, **807**, 173
- Hansen T., et al., 2015b, *ApJ*, **807**, 173
- Hansen C. J., El-Souri M., Monaco L., Villanova S., Bonifacio P., Caffau E., Sbordone L., 2018a, *ApJ*, **855**, 83
- Hansen T. T., et al., 2018b, *ApJ*, **858**, 92
- Harris C. R., et al., 2020, *Nature*, **585**, 357
- Hawkins K., Wyse R. F. G., 2018, *MNRAS*, **481**, 1028
- Hayek W., et al., 2009, *A&A*, **504**, 511
- Heiter U., et al., 2015, *Phys. Scr.*, **90**, 054010
- Herwig F., 2005, *ARA&A*, **43**, 435
- Herwig F., Pignatari M., Woodward P. R., Porter D. H., Rockefeller G., Fryer C. L., Bennett M., Hirschi R., 2011, *ApJ*, **727**, 89
- Hill V., et al., 2002, *A&A*, **387**, 560
- Hill V., Christlieb N., Beers T. C., Barklem P. S., Kratz K. L., Nordström B., Pfeiffer B., Farouqi K., 2017, *A&A*, **607**, A91
- Hirai Y., Ishimaru Y., Saitoh T. R., Fujii M. S., Hidaka J., Kajino T., 2015, *ApJ*, **814**, 41
- Hirai Y., Beers T. C., Chiba M., Aoki W., Shank D., Saitoh T. R., Okamoto T., Makino J., 2022, *MNRAS*, **517**, 4856
- Hollek J. K., Frebel A., Roederer I. U., Sneden C., Shetrone M., Beers T. C., Kang S.-j., Thom C., 2011, *ApJ*, **742**, 54
- Holmbeck E. M., et al., 2018, *The Astrophysical Journal*, **859**, L24
- Holmbeck E. M., Frebel A., McLaughlin G. C., Mumpower M. R., Sprouse T. M., Surman R., 2019, *The Astrophysical Journal*, **881**, 5
- Holmbeck E. M., et al., 2020, *ApJS*, **249**, 30
- Honda S., Aoki W., Kajino T., Ando H., Beers T. C., Izumiura H., Sadakane K., Takada-Hidai M., 2004, *ApJ*, **607**, 474
- Howes L. M., et al., 2015, *Nature*, **527**, 484
- Howes L. M., et al., 2016, *MNRAS*, **460**, 884
- Hunter J. D., 2007, *Computing in Science & Engineering*, **9**, 90
- Ishigaki M., Chiba M., Aoki W., 2010, *PASJ*, **62**, 143
- Ishigaki M. N., Aoki W., Chiba M., 2013, *ApJ*, **771**, 67
- Ivans I. I., Simmerer J., Sneden C., Lawler J. E., Cowan J. J., Gallino R., Bisterzo S., 2006, *ApJ*, **645**, 613
- Jacobson H. R., et al., 2015, *ApJ*, **807**, 171
- Ji A. P., Frebel A., 2018, *The Astrophysical Journal*, **856**, 138
- Ji A. P., Frebel A., Simon J. D., Chiti A., 2016, *ApJ*, **830**, 93
- Ji A. P., et al., 2022, arXiv e-prints, p. arXiv:2207.03499
- Johnson J. A., 2002a, *ApJS*, **139**, 219
- Johnson J. A., 2002b, *ApJS*, **139**, 219
- Johnson J. A., Bolte M., 2001, *ApJ*, **554**, 888
- Johnson C. I., McWilliam A., Rich R. M., 2013, *ApJ*, **775**, L27
- Jones S., Ritter C., Herwig F., Fryer C., Pignatari M., Bertolli M. G., Paxton B., 2016, *MNRAS*, **455**, 3848
- Jonsell K., Edvardsson B., Gustafsson B., Magain P., Nissen P. E., Asplund M., 2005, *A&A*, **440**, 321
- Kupka F., Piskunov N., Ryabchikova T. A., Stempels H. C., Weiss W. W., 1999, *A&AS*, **138**, 119
- Kurucz R., 1993, ATLAS9 Stellar Atmosphere Programs and 2 km/s grid. Kurucz CD-ROM No. 13. Cambridge, 13
- Lai D. K., Johnson J. A., Bolte M., Lucatello S., 2007, *ApJ*, **667**, 1185
- Lai D. K., Bolte M., Johnson J. A., Lucatello S., Heger A., Woosley S. E., 2008, *ApJ*, **681**, 1524
- Lambert D. L., Sneden C., 1977, *ApJ*, **215**, 597
- Langer N., Arcoragi J. P., Arnould M., 1986, *Mitteilungen der Astronomischen Gesellschaft Hamburg*, **67**, 334
- Lattimer J. M., Schramm D. N., 1974, *ApJ*, **192**, L145
- Lattimer J. M., Schramm D. N., 1976, *ApJ*, **210**, 549
- Lawler J. E., Wickliffe M. E., Cowley C. R., Sneden C., 2001a, *ApJS*, **137**, 341
- Lawler J. E., Bonvallet G., Sneden C., 2001b, *ApJ*, **556**, 452
- Lawler J. E., Wickliffe M. E., den Hartog E. A., Sneden C., 2001c, *ApJ*, **563**, 1075
- Lawler J. E., Sneden C., Cowan J. J., 2004, *ApJ*, **604**, 850
- Lawler J. E., Den Hartog E. A., Labby Z. E., Sneden C., Cowan J. J., Ivans I. I., 2006, arXiv e-prints, pp astro-ph/0611036
- Lawler J. E., Sneden C., Cowan J. J., Wyart J. F., Ivans I. I., Sobeck J. S., Stocke M. H., Den Hartog E. A., 2008, *ApJS*, **178**, 71
- Lawler J. E., Wood M. P., Den Hartog E. A., Feigenson T., Sneden C., Cowan J. J., 2014, *ApJS*, **215**, 20
- Lawler J. E., Hala Sneden C., Nave G., Wood M. P., Cowan J. J., 2019, *ApJS*, **241**, 21
- Leenaarts J., Carlsson M., Rouppe van der Voort L., 2012, *ApJ*, **749**, 136
- Li H.-N., Aoki W., Honda S., Zhao G., Christlieb N., Suda T., 2015a, *Research in Astronomy and Astrophysics*, **15**, 1264
- Li H.-N., Zhao G., Christlieb N., Wang L., Wang W., Zhang Y., Hou Y., Yuan H., 2015b, *ApJ*, **798**, 110
- Lind K., Asplund M., Barklem P. S., Belyaev A. K., 2011, *A&A*, **528**, A103
- Ljung G., Nilsson H., Asplund M., Johansson S., 2006, *A&A*, **456**, 1181
- Malcheva G., Blagoev K., Mayo R., Ortiz M., Xu H. L., Svanberg S., Quinet P., Biémont E., 2006, *MNRAS*, **367**, 754
- Mardini M. K., et al., 2019, *ApJ*, **875**, 89
- Marigo P., Bressan A., Nanni A., Girardi L., Pumo M. L., 2013, *MNRAS*, **434**, 488
- Mashonkina L., Christlieb N., Barklem P. S., Hill V., Beers T. C., Velichko A., 2010, *A&A*, **516**, A46
- Mashonkina L., Christlieb N., Eriksson K., 2014, *A&A*, **569**, A43
- Masseron T., et al., 2014, *A&A*, **571**, A47
- Matsuno T., Aoki W., Beers T. C., Lee Y. S., Honda S., 2017, *AJ*, **154**, 52
- McWilliam A., 1997, *ARA&A*, **35**, 503
- McWilliam A., 1998, *AJ*, **115**, 1640
- McWilliam A., Preston G. W., Sneden C., Searle L., 1995, *AJ*, **109**, 2757
- Mendoza C., Eissner W., LeDourneuf M., Zeippen C. J., 1995, *Journal of Physics B Atomic Molecular Physics*, **28**, 3485
- Metzger B. D., 2017, arXiv e-prints, p. arXiv:1710.05931
- Meyer B. S., 1989, *ApJ*, **343**, 254
- Mishenina T., et al., 2017, *MNRAS*, **469**, 4378
- Molina R. E., Giridhar S., Pereira C. B., Arellano Ferro A., Munee S., 2014, *Rev. Mex. Astron. Astrofis.*, **50**, 293
- Nagataki S., Takahashi R., Mizuta A., Takiwaki T., 2007, *ApJ*, **659**, 512
- Nilsson H., Zhang Z. G., Lundberg H., Johansson S., Nordström B., 2002, *A&A*, **382**, 368

- Nitz D. E., Kunau A. E., Wilson K. L., Lentz L. R., 1999, *ApJS*, **122**, 557
- Ou X., Roederer I. U., Sneden C., Cowan J. J., Lawler J. E., Shectman S. A., Thompson I. B., 2020, *ApJ*, **900**, 106
- Palmeri P., Quinet P., Wyart J. F., Biémont E., 2000, *Phys. Scr.*, **61**, 323
- Placco V. M., Frebel A., Beers T. C., Christlieb N., Lee Y. S., Kennedy C. R., Rossi S., Santucci R. M., 2014a, *ApJ*, **781**, 40
- Placco V. M., Frebel A., Beers T. C., Stancliffe R. J., 2014b, *ApJ*, **797**, 21
- Placco V. M., et al., 2017, *ApJ*, **844**, 18
- Placco V. M., et al., 2020, *ApJ*, **897**, 78
- Plez B., 2012, Turbospectrum: Code for spectral synthesis (ascl:1205.004)
- Plez B., Cohen J. G., 2005, *A&A*, **434**, 1117
- Prantzos N., Hashimoto M., Nomoto K., 1990, *A&A*, **234**, 211
- Preston G. W., Thompson I. B., Sneden C., Stachowski G., Shectman S. A., 2006, *AJ*, **132**, 1714
- Quinet P., Palmeri P., Biémont É., Jorissen A., van Eck S., Svanberg S., Xu H. L., Plez B., 2006, *A&A*, **448**, 1207
- Raiteri C. M., Busso M., Gallino R., Picchio G., 1991, *ApJ*, **371**, 665
- Ralchenko Y., Kramida A., Gillaspay J. D., Reader J., Fischer C. F., 2014, Determination of atomic data pertinent to the Fusion Energy Science Program, doi:10.2172/1149577, <https://www.osti.gov/biblio/1149577>
- Rasmussen K. C., Zepeda J., Beers T. C., Placco V. M., Depagne É., Frebel A., Dietz S., Hartwig T., 2020, *ApJ*, **905**, 20
- Reddy A. B. S., Giridhar S., Lambert D. L., 2012, *MNRAS*, **419**, 1350
- Ren J., Christlieb N., Zhao G., 2012, *A&A*, **537**, A118
- Roederer I. U., Lawler J. E., 2012, *ApJ*, **750**, 76
- Roederer I. U., Sneden C., Thompson I. B., Preston G. W., Shectman S. A., 2010a, *ApJ*, **711**, 573
- Roederer I. U., Cowan J. J., Karakas A. I., Kratz K.-L., Lugaro M., Simmerer J., Farouqi K., Sneden C., 2010b, *ApJ*, **724**, 975
- Roederer I. U., Preston G. W., Thompson I. B., Shectman S. A., Sneden C., Burley G. S., Kelson D. D., 2014a, *AJ*, **147**, 136
- Roederer I. U., Preston G. W., Thompson I. B., Shectman S. A., Sneden C., Burley G. S., Kelson D. D., 2014b, *AJ*, **147**, 136
- Roederer I. U., Preston G. W., Thompson I. B., Shectman S. A., Sneden C., 2014c, *ApJ*, **784**, 158
- Roederer I. U., et al., 2016, *AJ*, **151**, 82
- Roederer I. U., Sakari C. M., Placco V. M., Beers T. C., Ezzeddine R., Frebel A., Hansen T. T., 2018, *ApJ*, **865**, 129
- Rosswog S., Korobkin O., Arcones A., Thielemann F. K., Piran T., 2014, *MNRAS*, **439**, 744
- Ryabchikova T. A., Savanov I. S., Hatzes A. P., Weiss W. W., Handler G., 2000, *A&A*, **357**, 981
- Ryan S. G., Norris J. E., Bessell M. S., 1991, *AJ*, **102**, 303
- Ryan S. G., Norris J. E., Beers T. C., 1996, *ApJ*, **471**, 254
- Sakari C. M., et al., 2018a, *ApJ*, **854**, L20
- Sakari C. M., et al., 2018b, *ApJ*, **868**, 110
- Schatz H., Toenjes R., Pfeiffer B., Beers T. C., Cowan J. J., Hill V., Kratz K.-L., 2002, *ApJ*, **579**, 626
- Schlafly E. F., Finkbeiner D. P., 2011, *ApJ*, **737**, 103
- Shank D., et al., 2023, *ApJ*, **943**, 23
- Shappee B. J., et al., 2017, *Science*, **358**, 1574
- Shi J. R., Gehren T., Butler K., Mashonkina L. I., Zhao G., 2008, *A&A*, **486**, 303
- Short C. I., Hauschildt P. H., 2006, *ApJ*, **641**, 494
- Siegel D. M., Metzger B. D., 2018, *ApJ*, **858**, 52
- Siegel D. M., Barnes J., Metzger B. D., 2019, *Nature*, **569**, 241
- Siqueira Mello C., et al., 2014, *A&A*, **565**, A93
- Siqueira-Mello C., Andrievsky S. M., Barbuy B., Spite M., Spite F., Korotin S. A., 2015, *A&A*, **584**, A86
- Smartt S. J., et al., 2017, *Nature*, **551**, 75
- Sneden C., Pilachowski C. A., Vandenberg D. A., 1986, *ApJ*, **311**, 826
- Sneden C., Cowan J. J., Burris D. L., Truran J. W., 1998, *The Astrophysical Journal*, **496**, 235
- Sneden C., Cowan J. J., Ivans I. I., Fuller G. M., Burles S., Beers T. C., Lawler J. E., 2000, *ApJ*, **533**, L139
- Sneden C., Cowan J. J., Gallino R., 2008, *ARA&A*, **46**, 241
- Sneden C., Lawler J. E., Cowan J. J., Ivans I. I., Den Hartog E. A., 2009a, *ApJS*, **182**, 80
- Sneden C., Lawler J. E., Cowan J. J., Ivans I. I., Den Hartog E. A., 2009b, *ApJS*, **182**, 80
- Sneden C., Lawler J. E., Cowan J. J., Ivans I. I., Den Hartog E. A., 2009c, *ApJS*, **182**, 80
- Sneden C., Lucatello S., Ram R. S., Brooke J. S. A., Bernath P., 2014, *ApJS*, **214**, 26
- Sneden C., Cowan J. J., Kobayashi C., Pignatari M., Lawler J. E., Den Hartog E. A., Wood M. P., 2016, *ApJ*, **817**, 53
- Sousa S. G., Santos N. C., Israelian G., Mayor M., Monteiro M. J. P. F. G., 2007, *A&A*, **469**, 783
- Spite M., et al., 2005, *A&A*, **430**, 655
- Spite F., Spite M., Barbuy B., Bonifacio P., Caffau E., François P., 2018, *A&A*, **611**, A30
- Suda T., et al., 2008, *PASJ*, **60**, 1159
- Sumiyoshi K., Terasawa M., Mathews G. J., Kajino T., Yamada S., Suzuki H., 2001, *ApJ*, **562**, 880
- Symbalisty E., Schramm D. N., 1982, *Astrophys. Lett.*, **22**, 143
- Tabernero H. M., et al., 2020, *MNRAS*, **498**, 4222
- Takahashi K., Witti J., Janka H. T., 1994, *A&A*, **286**, 857
- Takeda Y., et al., 2002, *PASJ*, **54**, 765
- Tanaka M., et al., 2017, *PASJ*, **69**, 102
- Tanvir N. R., et al., 2017, *ApJ*, **848**, L27
- Tarumi Y., Hotokezaka K., Beniamini P., 2021, *ApJ*, **913**, L30
- Travaglio C., Gallino R., Arnone E., Cowan J., Jordan F., Sneden C., 2004, *ApJ*, **601**, 864
- Truran J. W., Iben I. J., 1977, *ApJ*, **216**, 797
- Valentini M., et al., 2019, *A&A*, **627**, A173
- Vejar G., Schuler S. C., Stassun K. G., 2021, *ApJ*, **919**, 100
- Villar V. A., et al., 2017, *ApJ*, **851**, L21
- Wanajo S., Tamamura M., Itoh N., Nomoto K., Ishimaru Y., Beers T. C., Nozawa S., 2003, *ApJ*, **593**, 968
- Wanajo S., Müller B., Janka H.-T., Heger A., 2018, *ApJ*, **852**, 40
- Watson D., et al., 2019, *Nature*, **574**, 497
- Wehmeyer B., Pignatari M., Thielemann F. K., 2015, *MNRAS*, **452**, 1970
- Wes McKinney 2010, in Stéfan van der Walt Jarrod Millman eds, Proceedings of the 9th Python in Science Conference. pp 56 – 61, doi:10.25080/Majora-92bf1922-00a
- Westin J., Sneden C., Gustafsson B., Cowan J. J., 2000, *ApJ*, **530**, 783
- Wheeler J. C., Cowan J. J., Hillebrandt W., 1998, *ApJ*, **493**, L101
- Wood M. P., Lawler J. E., Den Hartog E. A., Sneden C., Cowan J. J., 2014, *ApJS*, **214**, 18
- Woosley S. E., 1993, *ApJ*, **405**, 273
- Woosley S. E., Hoffman R. D., 1992, *ApJ*, **395**, 202
- Xing Q.-F., Zhao G., Aoki W., Honda S., Li H.-N., Ishigaki M. N., Matsuno T., 2019, *Nature Astronomy*, **3**, 631
- Yong D., et al., 2013, *ApJ*, **762**, 26
- Yong D., et al., 2014, *MNRAS*, **441**, 3396
- Yong D., et al., 2021, *Nature*, **595**, 223
- Zhang Z. G., Svanberg S., Jiang Z., Palmeri P., Quinet P., Quinet P., Biémont E., 2001, *Phys. Scr.*, **63**, 122
- Zhang L., Ishigaki M., Aoki W., Zhao G., Chiba M., 2009, *ApJ*, **706**, 1095
- Şahin T., Lambert D. L., 2009, *MNRAS*, **398**, 1730
- pandas development team T., 2020, pandas-dev/pandas: Pandas, doi:10.5281/zenodo.3509134, <https://doi.org/10.5281/zenodo.3509134>

APPENDIX A: ELEMENTAL ABUNDANCES OF ELEMENTS

In Tables A1, A2, A3, and A4, we list the elemental abundances derived for TYC 3431-689-1, HD 263815, TYC 1716-1548-1 and TYC 1191-918-1 respectively. Each table contains the name of the element, the atomic/molecular species used for abundance estimation, the atomic number, the number of lines used for abundance estimation, the solar abundances of the corresponding element, the abundance of the program star from the spectral-synthesis method (except for Ti, for which we have plenty of clear lines available), the relative abundance of program star with respect to the solar value and with respect to Fe ([X/Fe]), and the uncertainty in the abundance estimation. Whenever possible, for the relative abundance, we have consider absolute abundance obtained from the spectral-synthesis method.

APPENDIX B: Fe-I AND Fe-II LINES INFORMATION

Table B1 provides a complete Fe I and Fe II line list for all the program stars. It includes the elemental ionization, wavelength, lower excitation potential (LEP), and $\log g f$. The equivalent widths of lines identified in the spectra are listed under corresponding program star. References of the $\log g f$ values for these lines are written below the Table B1.

Table A1. Detailed abundance determination for TYC 3431-689-1.

Element	species	atomic no.	N-lines	Solar	A(X) _{syn}	[X/H]	[X/Fe]	σ
C	CH	6	1	8.39	5.74	-2.65	-0.60	0.23
N	CN	7	1	7.78	6.78	-1.00	+1.05	0.18
Na	Na I	11	2	6.17	4.72	-1.45	+0.60	0.25
Mg	Mg I	12	7	7.53	5.93	-1.60	+0.45	0.17
Al	Al I	13	2	6.37	4.17	-2.20	-0.15	0.14
Si	Si I	14	2	7.51	5.71	-1.80	+0.25	0.13
Ca	Ca I	20	14	6.31	4.6	-1.71	+0.34	0.12
Sc	Sc I	21	1	3.17	0.67	-2.50	-0.45	0.31
Sc	Sc II	21	9	3.17	1.07	-2.10	-0.05	0.10
Ti	Ti I	22	18	4.90	3.07	-1.83	+0.22	0.19
Ti	Ti II	22	31	4.90	3.18	-1.72	+0.33	0.08
V	V I	23	4	4.00	1.6	-2.40	-0.35	0.23
V	V II	23	2	4.00	1.9	-2.10	-0.05	0.11
Cr	Cr I	24	13	5.64	3.31	-2.33	-0.28	0.19
Cr	Cr II	24	5	5.64	3.54	-2.10	-0.05	0.08
Mn	Mn I	25	8	5.39	2.82	-2.57	-0.52	0.19
Co	Co I	27	3	4.92	3.02	-1.90	+0.15	0.24
Ni	Ni I	28	16	6.23	4.03	-2.20	-0.15	0.13
Cu	Cu I	29	1	4.21	1.05	-3.16	-1.11	0.19
Zn	Zn I	30	2	4.60	2.65	-1.95	+0.10	0.08
Sr	Sr II	38	2	2.92	1.02	-1.90	+0.15	0.13
Y	Y II	39	7	2.21	0.01	-2.20	-0.15	0.10
Zr	Zr II	40	7	2.58	0.88	-1.70	+0.35	0.10
Ba	Ba II	56	5	2.17	0.37	-1.80	+0.25	0.13
La	La II	57	4	1.13	-0.57	-1.70	+0.35	0.11
Ce	Ce II	58	3	1.70	-0.35	-2.05	+0.00	0.12
Pr	Pr II	59	1	0.58	-0.72	-1.30	+0.75	0.07
Nd	Nd II	60	6	1.45	-0.12	-1.57	+0.48	0.12
Sm	Sm II	62	3	1.00	-0.5	-1.50	+0.55	0.12
Eu	Eu II	63	2	0.52	-0.73	-1.25	+0.80	0.03
Gd	Gd II	64	2	1.11	-0.39	-1.50	+0.55	0.15
Tb	Tb II	65	1	0.28	-0.82	-1.10	+0.95	0.23
Dy	Dy II	66	3	1.14	-0.29	-1.43	+0.62	0.12
Ho	Ho II	67	1	0.51	-0.69	-1.20	+0.85	0.02
Er	Er II	68	2	0.93	-0.57	-1.50	+0.55	0.11
Lu	Lu II	71	1	0.06	-1.24	-1.30	+0.75	0.12
Hf	Hf II	72	2	0.88	-0.72	-1.60	+0.45	0.15
Os	Os I	76	2	1.25	-0.15	-1.40	+0.65	0.21
Pb	Pb II	82	1	2.00	<0.1	—	—	—
Th	Th II	90	1	0.06	-1.34	-1.40	+0.65	0.1

Table A2. Detailed abundance determination for HD 263815.

Element	species	atomic no.	N-lines	Solar	$A(X)_{\text{syn}}$	[X/H]	[X/Fe]	σ
C	CH	6	1	8.39	5.59	-2.80	-0.58	0.25
N	CN	7	1	7.78	6.28	-1.50	+0.72	0.18
Na	Na I	11	2	6.17	4.22	-1.95	+0.27	0.26
Mg	Mg I	12	7	7.53	5.83	-1.70	+0.52	0.17
Al	Al I	13	2	6.37	3.87	-2.50	-0.28	0.15
Si	Si I	14	2	7.51	5.71	-1.80	+0.42	0.11
Ca	Ca I	20	14	6.31	4.43	-1.88	+0.34	0.14
Sc	Sc I	21	1	3.17	0.39	-2.78	-0.56	0.31
Sc	Sc II	21	9	3.17	0.96	-2.21	+0.01	0.09
Ti	Ti I	22	14	4.90	2.9	-2.00	+0.22	0.19
Ti	Ti II	22	33	4.90	3.0	-1.90	+0.32	0.08
V	V I	23	4	4.00	1.50	-2.50	-0.28	0.24
V	V II	23	3	4.00	1.90	-2.10	+0.12	0.08
Cr	Cr I	24	13	5.64	3.12	-2.52	-0.30	0.22
Cr	Cr II	24	5	5.64	3.44	-2.20	+0.02	0.06
Mn	Mn I	25	8	5.39	2.66	-2.73	-0.51	0.21
Co	Co I	27	3	4.92	2.92	-2.00	+0.22	0.27
Ni	Ni I	28	16	6.23	4.08	-2.15	+0.07	0.14
Cu	Cu I	29	1	4.21	1.01	-3.20	-0.98	0.21
Zn	Zn I	30	2	4.60	2.55	-2.05	+0.17	0.05
Sr	Sr II	38	2	2.92	0.52	-2.40	-0.18	0.13
Y	Y II	39	7	2.21	-0.29	-2.50	-0.28	0.09
Zr	Zr II	40	7	2.58	0.48	-2.10	+0.12	0.14
Ba	Ba II	56	5	2.17	-0.18	-2.35	-0.13	0.13
La	La II	57	4	1.13	-1.04	-2.17	+0.05	0.12
Ce	Ce II	58	3	1.70	-0.8	-2.50	-0.28	0.14
Pr	Pr II	59	2	0.58	-1.02	-1.60	+0.62	0.1
Nd	Nd II	60	6	1.45	-0.51	-1.96	+0.26	0.13
Sm	Sm II	62	3	1.00	-1.00	-2.00	+0.22	0.13
Eu	Eu II	63	2	0.52	-1.18	-1.70	+0.52	0.01
Gd	Gd II	64	2	1.11	-0.79	-1.90	+0.32	0.14
Tb	Tb II	65	1	0.28	-1.22	-1.50	+0.72	0.2
Dy	Dy II	66	3	1.14	-0.86	-2.00	+0.22	0.16
Ho	Ho II	67	2	0.51	-1.19	-1.70	+0.52	0.01
Er	Er II	68	2	0.93	-0.97	-1.90	+0.32	0.14
Tm	Tm II	69	1	0.0	-1.5	-1.50	+0.72	0.1
Lu	Lu II	71	1	0.06	-1.54	-1.60	+0.62	0.14
Hf	Hf II	72	2	0.88	-1.02	-1.90	+0.32	0.14
Os	Os I	76	1	1.25	-0.45	-1.70	+0.52	0.22
Pb	Pb II	82	1	2.00	<-0.1	<-2.1	<0.12	—
Th	Th II	90	1	0.06	<-2.04	—	—	—

Table A3. Detailed abundance determination for TYC 1716-1548-1.

Element	species	atomic no.	N-lines	Solar	$A(X)_{\text{syn}}$	[X/H]	[X/Fe]	σ
C	CH	6	1	8.39	5.89	-2.50	-0.35	0.27
N	CN	7	1	7.78	6.58	-1.20	+0.95	0.20
Na	Na I	11	2	6.17	4.17	-2.00	+0.15	0.32
Mg	Mg I	12	7	7.53	5.9	-1.63	+0.52	0.23
Al	Al I	13	2	6.37	4.17	-2.20	-0.05	0.17
Si	Si I	14	2	7.51	5.81	-1.70	+0.45	0.15
Ca	Ca I	20	14	6.31	4.36	-1.95	+0.20	0.19
Sc	Sc I	21	1	3.17	0.46	-2.71	-0.56	0.3
Sc	Sc II	21	9	3.17	0.92	-2.25	-0.1	0.05
Ti	Ti I	22	15	4.90	2.92	-1.98	+0.17	0.28
Ti	Ti II	22	29	4.90	3.27	-1.63	+0.52	0.06
V	V I	23	4	4.00	1.55	-2.45	-0.30	0.28
Cr	Cr I	24	13	5.64	3.24	-2.40	-0.25	0.28
Cr	Cr II	24	5	5.64	3.49	-2.15	+0.00	0.09
Mn	Mn I	25	8	5.39	2.63	-2.76	-0.61	0.26
Co	Co I	27	3	4.92	2.72	-2.20	-0.05	0.29
Ni	Ni I	28	16	6.23	3.91	-2.32	-0.17	0.17
Cu	Cu I	29	1	4.21	1.08	-3.13	-0.98	0.26
Zn	Zn I	30	2	4.60	2.55	-2.05	+0.10	0.04
Ga	Ga I	31	1	2.88	0.48	-2.40	-0.25	—
Sr	Sr II	38	2	2.92	0.92	-2.00	+0.15	0.05
Y	Y II	39	7	2.21	0.01	-2.20	-0.05	0.07
Zr	Zr II	40	7	2.58	0.98	-1.60	+0.55	0.07
Ba	Ba II	56	7	2.17	0.19	-1.98	+0.17	0.04
La	La II	57	4	1.13	-0.72	-1.85	+0.30	0.07
Ce	Ce II	58	3	1.70	-0.55	-2.25	-0.10	0.08
Pr	Pr II	59	2	0.58	-0.42	-1.00	+1.15	0.1
Nd	Nd II	60	3	1.45	-0.05	-1.50	+0.65	0.07
Sm	Sm II	62	2	1.00	-0.75	-1.75	+0.40	0.1
Eu	Eu II	63	2	0.52	-0.83	-1.35	+0.80	0.02
Gd	Gd II	64	2	1.11	-0.49	-1.60	+0.55	0.17
Dy	Dy II	66	3	1.14	-0.43	-1.57	+0.58	0.09
Ho	Ho II	67	2	0.51	-0.99	-1.50	+0.65	0.1
Er	Er II	68	2	0.93	-0.47	-1.40	+0.75	0.13
Lu	Lu II	71	1	0.06	-1.33	-1.39	+0.76	0.11
Os	Os I	76	2	1.25	-0.15	-1.40	+0.75	0.19
Pb	Pb II	82	1	2.00	<0.1	<-1.9	<0.25	—

Table A4. Detailed abundance determination for TYC 1191-918-1.

Element	species	atomic no.	N-lines	Solar	A(X) _{syn}	[X/H]	[X/Fe]	σ
C	CH	6	1	8.39	5.79	-2.60	-0.70	0.24
N	CN	7	1	7.78	6.78	-1.00	+0.90	0.19
Na	Na I	11	2	6.17	4.47	-1.70	+0.20	0.26
Mg	Mg I	12	7	7.53	6.15	-1.38	+0.52	0.18
Al	Al I	13	2	6.37	4.07	-2.30	-0.40	0.13
Si	Si I	14	2	7.51	5.91	-1.60	+0.30	0.13
Ca	Ca I	20	14	6.31	4.72	-1.59	+0.31	0.15
Sc	Sc II	21	9	3.17	1.12	-2.05	-0.15	0.12
Ti	Ti I	22	17	4.90	3.19	-1.71	+0.19	0.23
Ti	Ti II	22	22	4.90	3.4	-1.50	+0.40	0.10
V	V I	23	4	4.00	1.81	-2.19	-0.29	0.24
V	V II	23	1	4.00	2.1	-1.90	+0.00	0.13
Cr	Cr I	24	13	5.64	3.44	-2.20	-0.30	0.24
Cr	Cr II	24	5	5.64	3.72	-1.92	-0.02	0.1
Mn	Mn I	25	8	5.39	2.89	-2.50	-0.60	0.17
Co	Co I	27	3	4.92	2.92	-2.00	-0.10	0.29
Ni	Ni I	28	16	6.23	4.20	-2.03	-0.13	0.15
Cu	Cu I	29	1	4.21	1.31	-2.90	-1.00	0.21
Zn	Zn I	30	2	4.60	2.70	-1.90	+0.00	0.07
Sr	Sr II	38	2	2.92	0.92	-2.00	-0.10	0.12
Y	Y II	39	7	2.21	0.21	-2.00	-0.10	0.13
Zr	Zr II	40	5	2.58	0.84	-1.74	+0.16	0.12
Ba	Ba II	56	3	2.17	0.13	-2.04	-0.14	0.15
La	La II	57	4	1.13	-0.52	-1.65	+0.25	0.14
Ce	Ce II	58	3	1.70	-0.35	-2.05	-0.15	0.15
Pr	Pr II	59	2	0.58	-0.82	-1.40	+0.50	0.12
Nd	Nd II	60	6	1.45	-0.08	-1.53	+0.37	0.15
Sm	Sm II	62	3	1.00	-0.6	-1.60	+0.30	0.14
Eu	Eu II	63	2	0.52	-0.83	-1.35	+0.55	0.03
Tb	Tb II	65	1	0.28	-1.82	-1.10	+0.80	0.12
Dy	Dy II	66	3	1.14	-0.39	-1.53	+0.37	0.15
Ho	Ho II	67	2	0.51	-0.89	-1.40	+0.50	0.13
Er	Er II	68	2	0.93	-0.58	-1.51	+0.39	0.12
Hf	Hf II	72	1	0.88	-0.82	-1.70	+0.20	0.16
Os	Os I	76	2	1.25	-0.1	-1.35	+0.55	0.21
Th	Th II	90	1	0.06	-1.24	-1.30	+0.60	0.12

Table B1: Information about the Fe line list.

Element	wavelength (Å)	EP (eV)	$\log g f$	TYC 3431-689-1	HD 263815	TYC 1716-1548-1	TYC 1191-918-1
Fe I	4107.488	2.831	-0.879	84.9	84.5	106.9	111.2
Fe I	4170.902	3.017	-1.086	81.7	78.9	86.5	111.9
Fe I	4174.913	0.915	-2.969	80.1	100.8	134.1	119.3
Fe I	4175.636	2.845	-0.827	74.9	81.8	96.6	104.1
Fe I	4182.383	3.017	-1.18	51.0	43.7	52.3	—
Fe I	4206.697	0.052	-3.96	110.3	—	156.8	153.6
Fe I	4216.22	2.453	-5.376	133.9	109.1	185.2	252.2
Fe I	4225.454	3.417	-0.51	104.2	—	131.5	—
Fe I	4233.603	2.482	-0.604	85.8	—	99.4	97.2
Fe I	4433.219	3.654	-0.7	34.5	33.5	51.3	54.7
Fe I	4433.782	3.602	-1.267	40.6	27.6	52.3	53.0
Fe I	4442.339	2.198	-1.255	98.4	99.3	119.3	90.0
Fe I	4447.717	2.223	-1.342	91.6	87.0	113.6	110.3
Fe I	4494.563	2.198	-1.136	101.2	103.6	121.4	128.2
Fe I	4517.525	3.071	-1.858	20.8	16.3	29.7	32.2
Fe I	4602.001	1.608	-3.154	35.7	39.7	69.5	60.9
Fe I	4602.941	1.485	-2.209	91.5	98.6	114.2	115.1
Fe I	4625.045	3.241	-1.34	35.3	38.0	53.3	57.2
Fe I	4632.912	1.608	-2.913	55.5	55.7	94.6	83.7
Fe I	4710.283	3.018	-1.612	33.9	36.3	46.5	58.5
Fe I	4733.592	1.485	-2.988	61.9	60.6	82.0	85.0
Fe I	4736.773	3.211	-0.752	67.4	68.8	90.3	90.9
Fe I	4871.318	2.865	-0.363	101.4	103.2	123.6	122.7
Fe I	4872.138	2.882	-0.567	95.5	94.8	119.5	93.8
Fe I	4890.755	2.875	-0.394	101.1	101.0	123.9	120.5
Fe I	4891.492	2.851	-0.112	107.8	116.1	131.2	127.2
Fe I	4903.31	2.882	-0.926	63.1	78.6	98.4	95.2
Fe I	4924.77	2.279	-2.241	46.2	51.0	69.8	70.8
Fe I	4939.687	0.859	-3.34	73.2	72.0	103.7	95.5
Fe I	4946.388	3.368	-1.17	36.6	29.7	63.9	53.8
Fe I	4982.524	4.103	0.144	43.3	42.6	49.4	54.7
Fe I	4994.13	0.915	-3.08	76.1	95.0	122.1	106.7
Fe I	5001.864	3.881	0.01	57.6	57.1	75.1	74.5
Fe I	5002.793	3.396	-1.58	21.8	20.1	34.6	29.5
Fe I	5014.943	3.943	-0.303	45.8	40.4	54.5	58.1
Fe I	5027.12	4.154	-0.559	34.8	29.7	46.3	50.5
Fe I	5039.252	3.368	-1.573	22.2	22.2	38.3	37.6
Fe I	5044.211	2.851	-2.038	32.1	23.6	38.6	39.9
Fe I	5049.82	2.279	-1.355	86.0	92.1	118.5	112.9
Fe I	5051.635	0.915	-2.795	108.1	111.7	140.2	129.2
Fe I	5060.079	0	-5.46	24.1	—	65.3	—
Fe I	5068.766	2.94	-1.042	68.0	66.1	113.3	87.0
Fe I	5079.74	0.99	-3.22	88.7	82.7	132.6	120.2
Fe I	5083.339	0.958	-2.958	94.1	101.9	133.9	121.7
Fe I	5090.774	4.256	-0.4	25.3	17.2	34.7	33.5
Fe I	5125.117	4.22	-0.14	43.5	31.2	55.6	60.4
Fe I	5127.359	0.915	-3.307	77.5	85.5	113.8	106.5
Fe I	5133.689	4.178	0.14	60.3	59.3	76.9	78.7
Fe I	5150.84	0.99	-3.003	80.9	88.6	114.5	108.5
Fe I	5162.273	4.178	0.02	55.8	49.4	71.9	69.5
Fe I	5166.282	0	-4.195	91.3	101.1	132.4	119.7
Fe I	5171.596	1.485	-1.793	113.9	105.9	150.9	133.9
Fe I	5191.455	3.038	-0.551	100.8	91.1	148.5	133.2
Fe I	5192.344	2.998	-0.421	90.2	88.4	122.9	114.9
Fe I	5194.942	1.557	-2.09	100.6	97.8	140.2	119.8
Fe I	5198.711	2.223	-2.135	59.5	58.4	89.7	85.4
Fe I	5202.336	2.176	-1.838	89.6	84.9	120.0	113.7
Fe I	5215.181	3.266	-0.871	48.7	51.5	66.8	68.8
Fe I	5216.274	1.608	-2.15	95.2	98.8	119.7	116.6

Fe I	5217.389	3.211	-1.07	44.2	45.3	69.0	66.6
Fe I	5225.526	0.11	-4.789	49.8	54.9	91.4	78.7
Fe I	5232.94	2.94	-0.058	110.4	115.5	131.1	131.8
Fe I	5247.05	0.087	-4.946	35.3	41.8	81.4	77.3
Fe I	5250.209	0.121	-4.938	30.0	-	60.6	57.9
Fe I	5250.646	2.198	-2.181	49.2	-	65.1	73.5
Fe I	5254.97	4.294	-4.035	63.5	65.8	100.4	97.2
Fe I	5263.306	3.266	-0.879	47.9	53.3	68.8	72.2
Fe I	5266.555	2.998	-0.386	91.4	96.6	116.3	112.3
Fe I	5281.79	3.038	-0.834	72.8	69.6	87.5	82.2
Fe I	5283.621	3.241	-0.432	67.9	-	89.4	84.8
Fe I	5322.041	2.279	-2.803	14.6	17.5	35.4	31.4
Fe I	5324.179	3.211	-0.103	105.5	100.8	126.5	122.9
Fe I	5332.9	1.557	-2.777	58.7	67.8	102.1	91.0
Fe I	5339.929	3.266	-0.647	62.2	68.6	86.9	87.5
Fe I	5367.467	4.415	0.443	50.0	47.5	60.4	64.0
Fe I	5369.962	4.371	0.536	59.6	55.8	70.5	75.4
Fe I	5383.369	4.312	0.645	62.0	63.6	72.3	79.4
Fe I	5389.479	4.415	-0.41	21.4	17.1	27.5	29.6
Fe I	5393.168	3.241	-0.715	65.0	66.8	88.8	83.8
Fe I	5397.128	0.915	-1.993	134.4	-	164.8	158.1
Fe I	5400.502	4.371	-0.16	34.6	27.2	42.5	42.1
Fe I	5415.199	4.386	0.642	66.6	56.3	74.0	76.7
Fe I	5445.042	4.386	-0.02	41.8	36.6	49.2	58.4
Fe I	5497.516	1.011	-2.849	101.7	110.5	133.6	-
Fe I	5501.465	0.958	-3.047	89.1	99.4	129.6	116.8
Fe I	5506.779	0.99	-2.797	105.2	109.8	131.9	127.9
Fe I	5572.842	3.396	-0.275	75.4	82.2	115.1	103.2
Fe I	5576.089	3.43	-1	57.8	48.8	67.8	72.2
Fe I	5586.822	3.695	-5.961	91.5	85.6	114.4	109.1
Fe I	5624.542	3.417	-0.755	57.0	50.5	68.6	73.8
Fe I	5762.992	4.209	-0.45	33.2	26.7	40.1	41.7
Fe I	5956.694	0.859	-4.605	22.5	19.1	56.5	38.8
Fe I	6065.482	2.608	-1.53	68.8	68.3	97.4	89.9
Fe I	6136.615	2.453	-1.4	91.8	92.3	144.4	134.9
Fe I	6137.692	2.588	-1.403	77.4	75.1	102.0	97.8
Fe I	6213.43	2.223	-2.482	45.4	38.7	70.7	58.5
Fe I	6230.723	2.559	-1.281	79.0	88.8	111.1	108.6
Fe I	6232.641	3.654	-1.223	23.6	19.4	25.8	32.7
Fe I	6246.319	3.602	-0.733	35.1	37.3	60.7	56.9
Fe I	6252.555	2.404	-1.687	79.2	75.6	96.3	97.1
Fe I	6265.134	2.176	-2.55	29.4	45.9	71.4	65.3
Fe I	6318.018	2.453	-2.338	51.3	52.0	74.6	83.7
Fe I	6393.601	2.433	-1.432	76.8	79.1	104.1	107.9
Fe I	6411.649	3.654	-0.595	43.1	47.7	70.0	69.9
Fe I	6421.351	2.279	-2.027	67.1	67.0	101.5	90.8
Fe I	6430.846	2.176	-2.006	75.8	73.9	105.7	95.4
Fe I	6592.914	2.727	-1.473	53.8	63.4	82.3	92.7
Fe I	6593.87	2.433	-2.422	35.3	38.1	69.9	58.1
Fe I	6663.442	2.424	-2.479	40.1	33.4	59.4	52.6
Fe I	6677.987	2.692	-1.418	74.4	68.2	114.7	94.0
Fe II	4233.172	2.583	-1.9	91.8	-	79.1	97.2
Fe II	4416.83	2.778	-2.41	70.8	69.5	72.1	85.8
Fe II	4489.183	2.828	-2.97	61.0	51.5	68.7	61.5
Fe II	4491.405	2.856	-2.7	60.7	58.6	69.1	73.6
Fe II	4508.288	2.856	-2.25	81.6	80.1	82.3	91.3
Fe II	4515.339	2.844	-2.45	68.2	74.4	71.5	88.2
Fe II	4520.224	2.807	-2.6	68.8	66.6	69.1	85.5
Fe II	4541.524	2.856	-2.79	44.7	45.8	38.5	65.5
Fe II	4582.835	2.844	-3.09	34.9	31.6	32.0	45.2
Fe II	4583.837	2.807	-1.86	92.9	94.2	98.3	111.9
Fe II	4620.521	2.828	-3.24	32.7	-	30.8	43.1

Fe II	4666.797	7.94	-3.798	30.6	27.7	36.5	46.0
Fe II	5197.568	10.398	-2.116	72.2	64.5	77.6	79.7
Fe II	5276.002	3.199	-1.94	87.4	80.7	90.4	94.0
Fe II	5362.869	3.199	-2.739	56.0	55.3	56.5	71.9
Fe II	6247.57	5.956	-4.011	30.23	23.0	28.7	30.0
Fe II	6456.383	3.903	-2.1	30.9	26.1	36.1	44.3

References for $\log g f$ values for Fe I and Fe II lines: Kupka et al. (1999) [VALD], Ralchenko et al. (2014) [NIST], Kurucz Linelist [<http://kurucz.harvard.edu/linelists.html>].

APPENDIX C: OTHER LINES LIST

In Table C1, we have listed a complete line list for elements other than Fe I and Fe II. The values of the lower excitation potential (LEP), and the $\log g f$ values listed in this table are adopted from the recent literature. Again, a checkmark represents the presence of a line in the spectra.

Table C1: Information about the line list.

Element	wavelength (Å)	EP (eV)	$\log g f$	TYC 3431-689-1	HD 263815	TYC 1716-1548-1	TYC 1191-918-1	Reference
Na I	5889.951	0.000	0.117	✓	✓	✓	✓	(1)
Na I	5895.924	0.000	-0.184	✓	✓	✓	✓	(1)
Mg I	5711.088	4.346	-1.833	✓	✓	✓	✓	(2)
Mg I	5528.405	4.346	-0.620	✓	✓	✓	✓	(2)
Mg I	5183.604	2.712	-0.180	✓	✓	✓	✓	(2)
Mg I	5172.684	2.712	-0.402	✓	✓	✓	✓	(2)
Mg I	4702.991	4.346	-0.666	✓	✓	✓	✓	(2)
Mg I	4571.096	0.000	-5.691	✓	✓	✓	✓	(2)
Mg I	4167.271	4.346	-1.004	✓	✓	✓	✓	(2)
Al I	3944.0	0.000	-0.640	✓	✓	✓	✓	(3)
Al I	3961.520	0.010	-0.340	✓	✓	✓	✓	(3)
Si I	4102.936	1.909	-3.140	✓	✓	✓	✓	(4)
Si I	6155.134	5.619	-0.400	✓	✓	✓	✓	(4)
Ca I	6493.781	2.521	-0.109	✓	✓	✓	✓	(5)
Ca I	6449.808	2.521	-1.015	✓	✓	✓	✓	(5)
Ca I	6439.075	2.526	0.394	✓	✓	✓	✓	(5)
Ca I	6102.723	1.879	-0.862	✓	✓	✓	✓	(5)
Ca I	5601.277	2.526	-0.552	✓	✓	✓	✓	(5)
Ca I	5588.749	2.526	0.313	✓	✓	✓	✓	(5)
Ca I	5590.114	2.521	-0.596	✓	✓	✓	✓	(5)
Ca I	5594.462	2.523	0.051	✓	✓	✓	✓	(5)
Ca I	5598.480	2.521	-0.134	✓	✓	✓	✓	(5)
Ca I	4578.551	2.521	-0.170	✓	✓	✓	✓	(5)
Ca I	4425.437	1.879	-0.286	✓	✓	✓	✓	(5)
Sc I*	4023.677	0.021	-	✓	✓	✓	✓	(6)
Sc II*	6245.637	1.507	-	✓	✓	✓	✓	(6)
Sc II*	5526.790	1.768	-	✓	✓	✓	✓	(6)
Sc II*	5239.813	1.455	-	✓	✓	✓	✓	(6)
Sc II*	5031.021	1.357	-	✓	✓	✓	✓	(6)
Sc II*	4670.407	1.357	-	✓	✓	✓	✓	(6)
Sc II*	4431.352	0.605	-	✓	✓	✓	✓	(6)
Sc II*	4324.996	0.595	-	✓	✓	✓	✓	(6)
Sc II*	4354.598	0.605	-	✓	✓	✓	✓	(6)
Sc II*	4415.557	0.595	-	✓	✓	✓	✓	(6)
Sc II*	4246.822	0.315	-	✓	✓	✓	✓	(6)
Sc II*	5641.001	1.500	-	✓	✓	✓	✓	(6)
Sc II*	5657.896	1.507	-	✓	✓	✓	✓	(6)
Sc II*	5657.896	1.507	-	✓	✓	✓	✓	(6)
Ti I	5336.848	1.582	-1.630	✓	✓	✓	✓	(7)
Ti I	5210.385	0.048	-0.884	✓	✓	✓	✓	(7)
Ti I	5193.881	2.345	-0.942	✓	✓	✓	✓	(7)
Ti I	5173.743	0.000	-1.118	✓	✓	✓	✓	(7)

Ti I	5036.464	1.443	0.130	✓	✓	✓	✓	(7)
Ti I	5038.397	1.430	0.013	✓	✓	✓	✓	(7)
Ti I	5040.613	0.826	-1.787	✓	✓	✓	✓	(7)
Ti I	5016.161	0.848	-0.574	✓	✓	✓	✓	(7)
Ti I	5020.026	0.836	-0.414	✓	✓	✓	✓	(7)
Ti I	5022.868	0.826	-0.434	✓	✓	✓	✓	(7)
Ti I	5024.844	0.818	-0.602	✓	✓	✓	✓	(7)
Ti I	4999.503	0.826	0.250	✓	✓	✓	✓	(7)
Ti I	4981.731	0.848	0.504	✓	✓	✓	✓	(7)
Ti I	4656.469	0.000	-1.345	✓	✓	✓	✓	(7)
Ti I	4617.269	1.749	0.389	✓	✓	✓	✓	(7)
Ti I	4623.097	1.739	0.110	✓	✓	✓	✓	(7)
Ti I	4534.776	0.836	0.280	✓	✓	✓	✓	(7)
Ti I	4533.241	0.848	0.476	✓	✓	✓	✓	(7)
Ti I	4512.734	0.836	-0.480	✓	✓	✓	✓	(7)
Ti I	4441.439	3.186	-1.792	✓	✓	✓	✓	(7)
Ti II	6491.561	2.061	-1.793	✓	✓	✓	✓	(7)
Ti II	5418.751	1.582	-2.110	✓	✓	✓	✓	(7)
Ti II	5490.690	1.566	-2.650	✓	✓	✓	✓	(7)
Ti II	5381.015	1.566	-1.970	✓	✓	✓	✓	(7)
Ti II	5211.536	2.590	-1.356	✓	✓	✓	✓	(7)
Ti II	5185.913	1.893	-1.370	✓	✓	✓	✓	(7)
Ti II	5188.680	1.582	-1.050	✓	✓	✓	✓	(7)
Ti II	5154.070	1.566	-1.920	✓	✓	✓	✓	(7)
Ti II	5129.152	1.892	-1.300	✓	✓	✓	✓	(7)
Ti II	5013.677	1.582	-1.990	✓	✓	✓	✓	(7)
Ti II	4911.193	3.124	-0.650	✓	✓	✓	✓	(7)
Ti II	4865.612	1.116	-2.810	✓	✓	✓	✓	(7)
Ti II	4805.085	2.061	-0.960	✓	✓	✓	✓	(7)
Ti II	4763.881	1.221	-2.360	✓	✓	✓	✓	(7)
Ti II	4779.985	2.048	-1.370	✓	✓	✓	✓	(7)
Ti II	4589.985	1.237	-1.620	✓	✓	✓	✓	(7)
Ti II	4568.314	1.224	-2.650	✓	✓	✓	✓	(7)
Ti II	4563.761	1.221	-0.790	✓	✓	✓	✓	(7)
Ti II	4544.028	1.243	-2.530	✓	✓	✓	✓	(7)
Ti II	4529.474	1.572	-1.650	✓	✓	✓	✓	(7)
Ti II	4493.513	1.080	-2.830	✓	✓	✓	✓	(7)
Ti II	4501.270	1.116	-0.760	✓	✓	✓	✓	(7)
Ti II	4443.801	1.080	-0.700	✓	✓	✓	✓	(7)
Ti II	4444.558	1.116	-2.210	✓	✓	✓	✓	(7)
Ti II	4411.074	3.095	-0.670	✓	✓	✓	✓	(7)
Ti II	4411.925	1.224	-2.550	✓	✓	✓	✓	(7)
Ti II	4394.051	1.221	-1.770	✓	✓	✓	✓	(7)
Ti II	4395.850	1.243	-1.970	✓	✓	✓	✓	(7)
V I*	4406.633	0.301	—	✓	✓	✓	✓	(8)
V I	4390.099	2.616	-1.504	✓	✓	✓	✓	(8)
V I*	4379.230	0.301	—	✓	✓	✓	✓	(8)
V I*	4111.774	0.301	—	✓	✓	✓	✓	(8)
V I*	4099.812	2.211	—	✓	✓	✓	✓	(8)
V II	4023.378	1.805	-0.689	✓	✓	✓	✓	(8)
V II	4036.777	1.476	-1.594	✓	✓	✓	✓	(8)
V II	4183.428	2.050	-1.112	✓	✓	✓	✓	(8)
Cr I	4646.148	1.030	-0.700	✓	✓	✓	✓	(9)
Cr I	4651.282	0.983	-1.460	✓	✓	✓	✓	(9)
Cr I	4652.152	1.004	-1.030	✓	✓	✓	✓	(9)
Cr I	4626.174	0.968	-1.320	✓	✓	✓	✓	(9)
Cr I	4616.120	0.983	-1.190	✓	✓	✓	✓	(9)
Cr I	5409.772	1.030	-0.720	✓	✓	✓	✓	(9)
Cr I	5345.801	1.004	-0.980	✓	✓	✓	✓	(9)
Cr I	5348.312	1.004	-1.290	✓	✓	✓	✓	(9)
Cr I	5296.691	0.983	-1.400	✓	✓	✓	✓	(9)
Cr I	5298.277	0.983	-1.150	✓	✓	✓	✓	(9)

Cr I	4591.457	3.422	-1.888	✓	✓	✓	✓	(9)
Cr I	4545.945	0.941	-1.370	✓	✓	✓	✓	(9)
Cr I	4254.332	0.000	-0.114	✓	✓	✓	✓	(9)
Cr II	4824.127	3.871	-0.970	✓	✓	✓	✓	(9)
Cr II	4634.070	4.072	-0.990	✓	✓	✓	✓	(9)
Cr II	4618.803	4.074	-0.840	✓	✓	✓	✓	(9)
Cr II	4588.199	4.071	-0.627	✓	✓	✓	✓	(9)
Cr II	4558.650	4.073	-0.449	✓	✓	✓	✓	(9)
Mn I*	4823.524	2.319	-	✓	✓	✓	✓	(10)
Mn I*	4783.427	2.298	-	✓	✓	✓	✓	(10)
Mn I*	4766.418	2.920	-	✓	✓	✓	✓	(10)
Mn I*	4754.042	2.282	-	✓	✓	✓	✓	(10)
Mn I*	4034.483	0.000	-	✓	✓	✓	✓	(10)
Mn I*	4033.062	0.000	-	✓	✓	✓	✓	(10)
Mn I*	4235.295	2.888	-	✓	✓	✓	✓	(10)
Mn I*	4041.355	2.114	-	✓	✓	✓	✓	(10)
Co I	4020.828	3.665	-0.961	✓	✓	✓	✓	(11)
Co I	4110.530	1.049	-1.080	✓	✓	✓	✓	(11)
Co I	4121.311	0.923	-0.320	✓	✓	✓	✓	(11)
Ni I	6643.629	1.676	-2.300	✓	✓	✓	✓	(12)
Ni I	6108.107	1.676	-2.450	✓	✓	✓	✓	(12)
Ni I	5155.762	3.898	0.011	✓	✓	✓	✓	(12)
Ni I	5115.389	3.834	-0.110	✓	✓	✓	✓	(12)
Ni I	5099.927	3.679	-0.100	✓	✓	✓	✓	(12)
Ni I	5080.528	3.655	0.330	✓	✓	✓	✓	(12)
Ni I	5081.107	3.847	0.300	✓	✓	✓	✓	(12)
Ni I	5035.357	3.635	0.290	✓	✓	✓	✓	(12)
Ni I	5017.568	3.539	-0.020	✓	✓	✓	✓	(12)
Ni I	4904.407	3.542	-0.170	✓	✓	✓	✓	(12)
Ni I	4866.262	3.539	-0.210	✓	✓	✓	✓	(12)
Ni I	4714.408	3.380	0.260	✓	✓	✓	✓	(12)
Ni I	4715.757	3.543	-0.320	✓	✓	✓	✓	(12)
Cu I*	5105.537	-	-	✓	✓	✓	✓	(13)
Zn I	4722.153	4.030	-0.338	✓	✓	✓	✓	(14)
Zn I	4810.528	4.078	-0.137	✓	✓	✓	✓	(14)
Sr II	4077.709	0.000	0.167	✓	✓	✓	✓	(15)
Sr II	4215.519	0.000	-0.145	✓	✓	✓	✓	(15)
Y II	4124.907	0.409	-1.500	✓	✓	✓	✓	(16)
Y II	4682.324	0.409	-1.510	✓	✓	✓	✓	(16)
Y II	4854.863	0.992	-0.11	✓	✓	✓	✓	(16)
Y II	4883.684	1.084	0.265	✓	✓	✓	✓	(16)
Y II	5087.416	1.084	-0.170	✓	✓	✓	✓	(16)
Y II	5123.211	0.992	-1.219	✓	✓	✓	✓	(16)
Y II	5200.406	0.992	-0.570	✓	✓	✓	✓	(16)
Y II	5662.925	1.944	0.38	✓	✓	✓	✓	(16)
Zr II	4029.684	0.713	-0.78	✓	✓	✓	✓	(17)
Zr II	4050.316	0.713	-1.000	✓	✓	✓	✓	(17)
Zr II	4090.535	0.758	-1.009	✓	✓	✓	✓	(17)
Zr II	4161.213	0.713	-0.59	✓	✓	✓	✓	(17)
Zr II	4150.986	0.802	-0.992	✓	✓	✓	✓	(17)
Zr II	4208.977	0.713	-0.460	✓	✓	✓	✓	(17)
Zr II	4211.907	0.527	-1.083	✓	✓	✓	✓	(17)
Zr II	4317.299	0.713	-1.450	✓	✓	✓	✓	(17)
Ba II	6496.897	0.604	-0.377	✓	✓	✓	✓	(18)
Ba II*	5853.700	-	-	✓	✓	✓	✓	(18)
Ba II*	6141.713	-	-	✓	✓	✓	✓	(18)
Ba II*	4554.033	-	-	✓	✓	✓	✓	(18)
Ba II*	4934.077	-	-	✓	✓	✓	✓	(18)
La II*	4333.753	-	-	✓	✓	✓	✓	(19)
La II*	4086.709	-	-	✓	✓	✓	✓	(19)
La II*	4123.218	-	-	✓	✓	✓	✓	(19)
La II	4921.776	0.244	-0.45	✓	✓	✓	✓	(19)

La II*	4322.503	–	–	✓	✓	✓	✓	(19)
Ce II	4186.594	0.864	0.74	✓	✓	✓	✓	(20)
Ce II	4562.359	0.478	0.23	✓	✓	✓	✓	(20)
Ce II	4486.909	0.295	–0.090	✓	✓	✓	✓	(20)
Ce II	4628.161	0.516	0.220	✓	✓	✓	✓	(20)
Pr II*	4143.11	–	–	✓	✓	–	✓	(21)
Pr II*	4179.39	–	–	✓	✓	–	✓	(21)
Nd II	4061.080	0.471	0.347	✓	✓	✓	✓	(22)
Nd II	4109.448	0.321	0.184	✓	✓	✓	✓	(22)
Nd II*	4232.374	–	–	✓	✓	✓	✓	(22)
Nd II	4135.321	0.631	–0.400	✓	✓	✓	✓	(22)
Nd II	4327.932	0.559	–0.430	✓	✓	✓	✓	(22)
Nd II	4338.690	0.742	–0.290	✓	✓	✓	✓	(22)
Nd II*	4358.161	–	–	✓	✓	✓	✓	(22)
Nd II	4825.478	0.182	–0.776	✓	✓	✓	✓	(22)
Sm II*	4424.337	–	–	✓	✓	✓	✓	(23)
Sm II	4434.318	0.378	–0.204	✓	✓	✓	✓	(23)
Sm II*	4467.341	–	–	✓	✓	✓	✓	(23)
Eu II*	4129.801	–	–	✓	✓	✓	✓	(24)
Eu II*	4205.05	–	–	✓	✓	✓	✓	(24)
Gd II	3850.97	0.000	–0.094	✓	✓	✓	–	(25)
Gd II	4037.33	0.662	–0.020	✓	✓	✓	–	(25)
Gd II	4085.6	0.731	–0.07	✓	✓	✓	–	(25)
Gd II	4098.61	0.819	0.312	✓	✓	✓	–	(25)
Tb II	3976.84	0.000	0.08	✓	✓	–	–	(26)
Dy II	4103.306	0.103	–0.390	✓	✓	✓	✓	(27)
Dy II	4111.343	0.000	–0.850	✓	✓	✓	✓	(27)
Dy II	4449.704	0.000	–1.030	✓	✓	✓	✓	(27)
Ho II	4045.44	0.000	–0.05	✓	✓	–	–	(28)
Ho II	4152.58	0.079	–0.930	✓	✓	–	–	(28)
Er II	3830.48	0.000	–0.22	✓	✓	✓	–	(29)
Er II	3896.23	0.055	–0.12	✓	✓	✓	–	(29)
Tm II	3848.02	0.000	–0.140	–	✓	–	–	(30)
Lu II	5476.69	1.760	–0.276	–	–	–	–	(31)
Hf II	3918.09	0.452	–1.14	✓	✓	–	✓	(32)
Hf II	4093.15	0.452	–1.15	✓	✓	–	✓	(32)
Os I	4260.85	0.000	–1.440	✓	✓	✓	✓	(33)
Os I	4420.47	0.000	–1.20	✓	✓	✓	✓	(33)
Pb I*	4057.8	–	–	–	–	–	–	(34)
Th II	4019.12	0.000	–0.228	✓	–	–	✓	(35)

References for log *g.f.*: (1) Sneden et al. (2014), (2) Sneden et al. (2014); Yong et al. (2014); Heiter et al. (2015), (3) Mendoza et al. (1995), (4) Shi et al. (2008), (5) Ryabchikova et al. (2000), (6) Lawler et al. (2019), (7) Kupka et al. (1999)[VALD]; Ralchenko et al. (2014)[NIST] (8) Lawler et al. (2014); Wood et al. (2014), (9) Kupka et al. (1999)[VALD]; Ralchenko et al. (2014)[NIST], (10) Den Hartog et al. (2011), (11) Nitz et al. (1999); Cardon et al. (1982), (12) Siqueira-Mello et al. (2015); Vejar et al. (2021) (13) Kurucz Linelist [<http://kurucz.harvard.edu/linelists.html>], (14) Takeda et al. (2002), (15) Mishenina et al. (2017), (16) Biémont et al. (2011) , (17) Ljung et al. (2006); Malcheva et al. (2006), (18) McWilliam 1998; Cui et al. 2013 , (19) Lawler et al. (2001b) , (20) Palmeri et al. (2000); Zhang et al. (2001), (21) Sneden et al. (2009a), (22) Kupka et al. (1999)[VALD], (23) Kupka et al. (1999)[VALD] , (24) Lawler et al. (2001c), (25) Kupka et al. (1999)[VALD] , (26) Lawler et al. (2001a), (27) Sneden et al. (2009b), (28) Lawler et al. (2004), (29) Lawler et al. (2008), (30) Sneden et al. (2009c), (31) Bord et al. (1997), (32) Lawler et al. (2006), (33) Quinet et al. (2006), (34) Roederer & Lawler (2012), (35) Nilsson et al. (2002).

Note: * with the name of element represents hyperfine splitting.

APPENDIX D: EVOLUTION OF HEAVY ELEMENTS WITH METALLICITY

Fig. D1 shows the evolution of all the heavy elements from Sr to Os as a function of metallicity. Similar to the main text, limited-*r* stars are shown in yellow colours, the *r*-I stars in cyan colours, and the *r*-II stars in magenta colours. The four black diamonds indicate the *r*-I (cyan) and *r*-II (magenta) program stars in this study. Fig. D2 shows the distribution of metallicity, [C/Fe], [Sr/H], and [Ba/H].

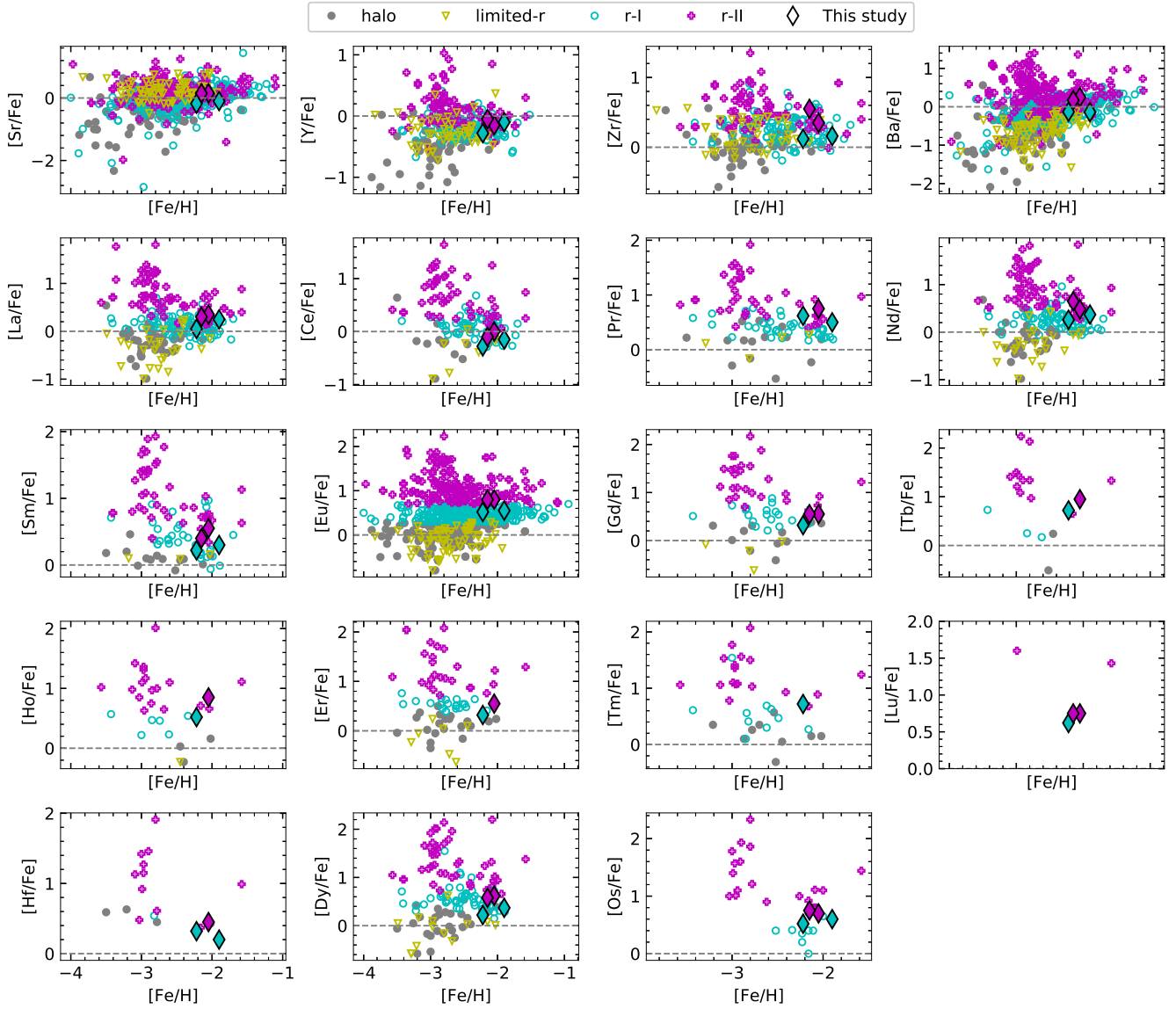


Figure D1. Abundance of heavy elements as a function of metallicity. The limited-*r* stars are shown in yellow colours, the *r*-I stars in cyan colours, and the *r*-II stars in magenta colours. The four black diamonds indicate the *r*-I (cyan) and *r*-II (magenta) program stars in this study. References for the *r*-process stars are given in the caption of Fig. 11. Normal metal-poor halo stars, shown with grey filled, are taken from Suda et al. (2008); Ryan et al. (1991); McWilliam et al. (1995); Burris et al. (2000); Fulbright (2000); Aoki et al. (2002); Johnson (2002a); Cayrel et al. (2004); Honda et al. (2004); Aoki et al. (2005); Barklem et al. (2005); Jonsell et al. (2005); Preston et al. (2006); Lai et al. (2007); Zhang et al. (2009); Ishigaki et al. (2010); Roederer et al. (2010a); Hollek et al. (2011); Allen et al. (2012); Aoki et al. (2013a); Cohen et al. (2013); Ishigaki et al. (2013); Yong et al. (2013); Placco et al. (2014a); Roederer et al. (2014a); Hansen et al. (2015b); Jacobson et al. (2015); Li et al. (2015b), and Abohalima & Frebel (2018).

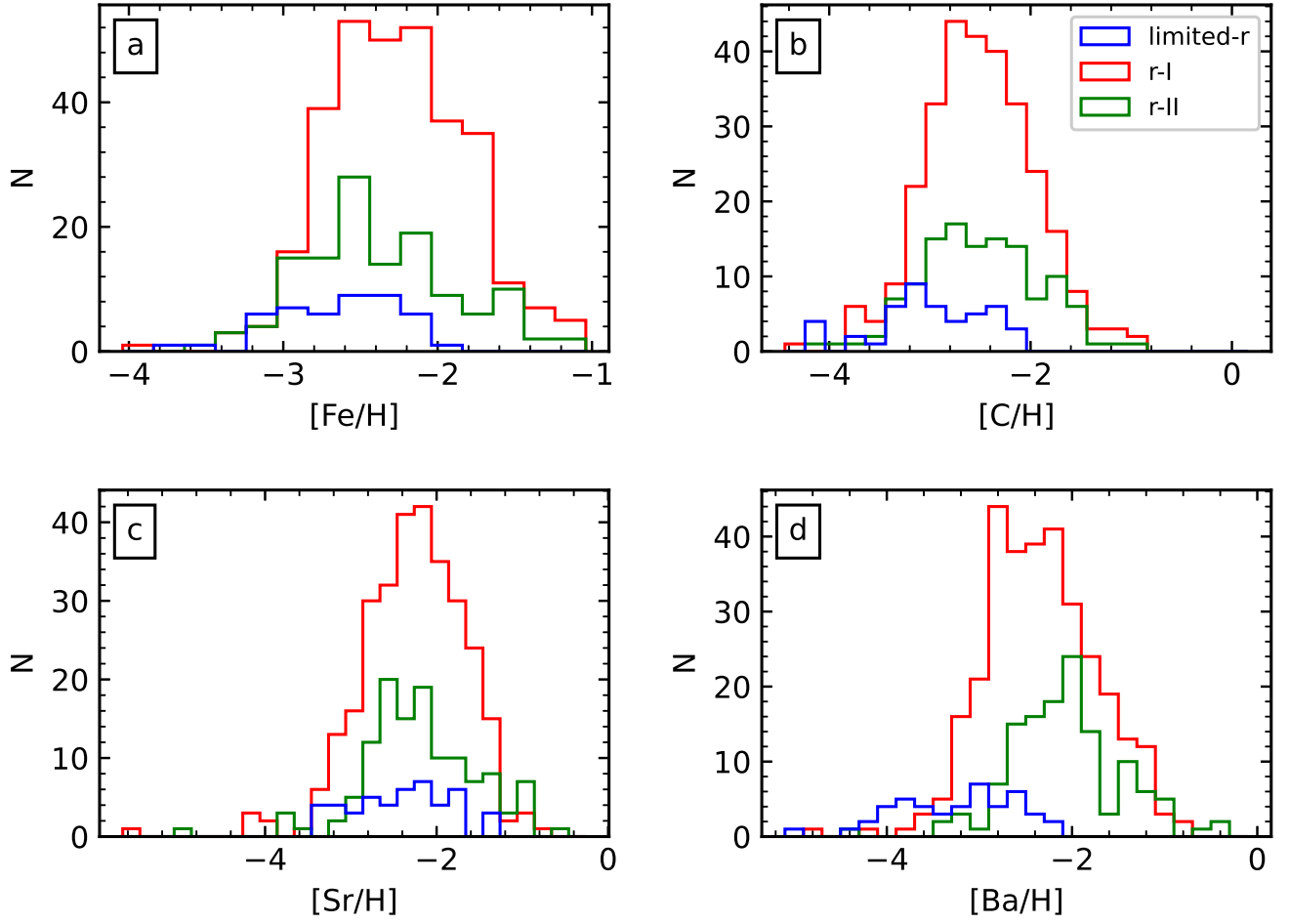


Figure D2. Comparison of metallicity, C, Sr, and Ba abundance distribution in RPE stars. The distribution of limited-*r* stars is shown with the blue histogram, the red histogram shows the distribution of *r*-I stars, and the green histogram displays the distribution of *r*-II stars. References for the RPE stars are given in the caption of Fig. 11.